JOURNAL OF GEOPHYSICAL RESEARCH, VOL. 100, NO. C5, PAGES 8791–8813, MAY 15, 1995

Tower-based measurements of normalized radar cross section from Lake Ontario: Evidence of wind stress dependence

Marie C. Colton
Satellite Division, Fleet Numerical Meteorology and Oceanography Center, Monterey, California

William J. Plant and William C. Keller
Applied Physics Laboratory, University of Washington, Seattle

Gerald L. Geernaert[1]
Scripps Institution of Oceanography, University of California, San Diego, La Jolla

Abstract. We report here the dependence of the normalized radar cross-section (NRCS) on incidence angle, azimuth angle, wind speed, wind stress, and atmospheric stratification for Ku band microwave backscatter from a lake. The measurements were made in autumn 1987 on Lake Ontario, using a rotating microwave system mounted on a research tower operated by the Canada Centre for Inland Waters. The results show that at intermediate incidence angles the NRCS on the lake generally increases faster with wind speed than it does on the ocean. We attribute this to the larger atmospheric drag coefficients which exist on the lake compared with the ocean, and we show that the results are more consistent with a dependence of the NRCS on wind stress than on wind speed near the surface. We find a stratification dependence of the NRCS similar to that previously reported at C band and show that at 40° and 60° incidence angles this dependence can be removed by parameterizing the NRCS in terms of either the friction velocity or neutral wind speed. At a 20° incidence angle the stratification dependence is not removed by this procedure.

1. Introduction

At intermediate incidence angles (20° to 70°), the normalized radar cross section (NRCS) for microwave backscatter from wind-roughened surfaces can be related by a "model function" to surface wind conditions. Most theories agree that this dependence is due primarily to "Bragg resonant" scattering of the incident radiation from short surface waves (0.2- to 20-cm wavelength). The backscattered power displays a strong angular dependence such that maxima occur when the antenna is pointed either upwind or downwind and minima occur when the antenna is pointed approximately cross wind. The upwind maximum is usually larger than the downwind maximum for any configuration of radar polarizations, and the difference is maximized for horizontally polarized radiation. This behavior is the basis for determining the wind vector over the sea by satellite scatterometry (see, for example, *Plant* [1990] and *Pierson* [1990] for a full derivation and details).

Previous model functions have been formulated by writing the NRCS of the sea as a function of wind speed at 19.5 m above the sea, radar incidence angle, azimuth angle relative to the true wind vector, and polarization [e.g., *Jones et al.*, 1977; *Moore and Fung*, 1979; *Schroeder et al.*, 1982; *Wentz et al.*, 1984]. However, *Daley et al.* [1984] identified deficiencies in this simple type of formulation and listed additional dependencies which may need to be included in the scatterometer model function to increase both its utility and physical consistency. On the basis of recent research, the NRCS may also depend upon the following factors: (1) dominant wave slope and direction relative to the wind vector [*Keller et al.*, 1985, 1989; *Li et al.*, 1989], (2) air-sea temperature differences, and thus the stratification of the marine surface layer [e.g., *Keller et al.*, 1985, 1989], (3) surface contaminants and films [*Hühnerfuss et al.*, 1983], (4) the viscosity of water as a function of temperature [*Woiceshyn*, 1986; *Donelan and Pierson*, 1987], and (5) marine boundary layer transients, inhomogeneity, and nonstationarity, for example, boundary layer rolls and coastal fronts [*Geernaert*, 1990, p. 94].

An increase in wind speed produces an associated increase in the NRCS through amplification of the gravity-capillary waves from which the electromagnetic waves are scattered. Observations show that the wind speed dependence can be represented fairly well as a simple power law for wind speeds greater than 4–5 m/s [*Jones et al.*, 1982; *Keller et al.*, 1992]. The cross section varies with wind direction as a result of the anisotropy of the gravity-capillary wave spectrum, and this behavior has been successfully modeled as a truncated Fourier cosine series [*Schroeder et al.*, 1982].

If the short waves are tilted toward and away from the radar and modulated in amplitude and frequency by the slope of the longer waves on which they ride, the NRCS will again be increased. Observational evidence for a long-wave influence has been reported by *Keller et al.* [1985, 1989], who

[1]Now at Division of Emissions and Air Pollution, National Environmental Research Institute, Roskilde, Denmark.

Paper number 95JC00364.
0148-0227/95/95JC-00364$05.00

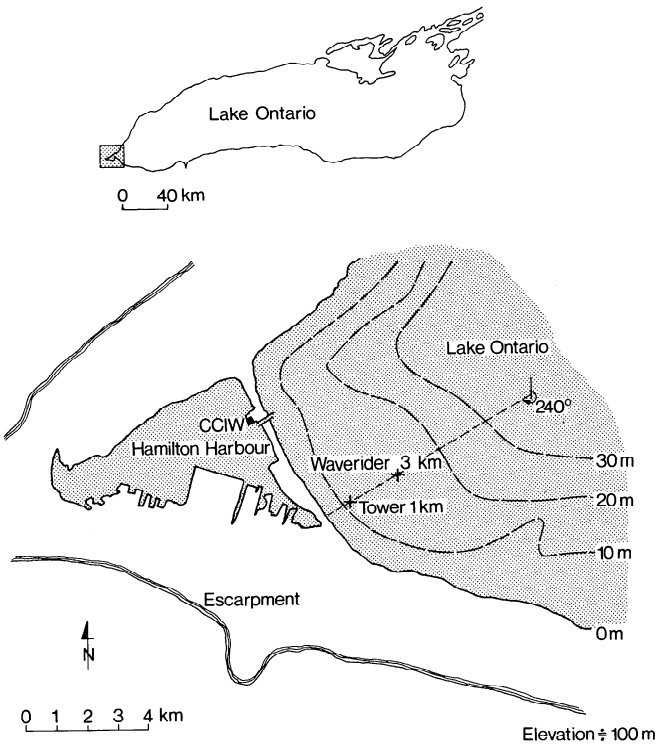

Figure 1. Map showing the location of the research tower in Lake Ontario. Courtesy of M. A. Donelan.

show that cross sections increase with wave slope only when the atmosphere is stably stratified. Measurements during neutral and unstable conditions yield no discernable dependence of the NRCS on long-wave slope.

To some extent, this daunting list of parameters that affect the NRCS can be reduced when applied to satellite scatterometry simply owing to the surface areas that are sampled. Global wind vectors obtained from scatterometry are usually specified with a 25- to 50-km spatial resolution, which averages out the effects of smaller-scale phenomena such as topographic interactions and most surfactants. Such spatial resolutions, and the requirement that footprints are not contaminated by coastal discontinuities, limit operational use of scatterometers to distances from shorelines that are beyond coastal fronts. Nevertheless, since phenomena affecting surface wave roughness can be due to processes acting over a large surface extent, a considerable number of parameters can still affect satellite-measured NRCS values.

One way to reduce the number of parameters responsible for the NRCS is to relate it to a surface parameter that also depends on surface waves, stratification, and films. Specifying the output of scatterometer model functions in terms of the wind stress could eliminate much of the dependence of the output on dominant wave properties, atmospheric stratification, and atmospheric rolls, since it is known that the wind stress is affected by these parameters in much the same way as the NRCS. The results of *Keller et al.* [1989] and *Askari et al.* [1993] suggest, via theoretical argument, that for equilibrium conditions the NRCS depends on wind stress. However, in their studies, direct measurements of the wind stress were not employed.

In this paper we report measurements made on Lake Ontario that shed light on the relevance of the wind stress to the behavior of the NRCS. Because the "younger" waves on the lake produce generally higher drag coefficients than the "older" waves of the ocean, surface stresses are different on the lake and on the ocean for the same wind speed. This produces differences in the behaviors of lake and ocean NRCS values, which may be used to investigate the possible wind parameters that could affect the NRCS. After we describe the experimental procedures in the next section and our methods of computing wind stress and neutral wind speed in section 3, we will show in section 4 that our measurements are more consistent with a dependence of the NRCS on wind stress than on wind speed at any arbitrary level below 19.5 m. In section 5

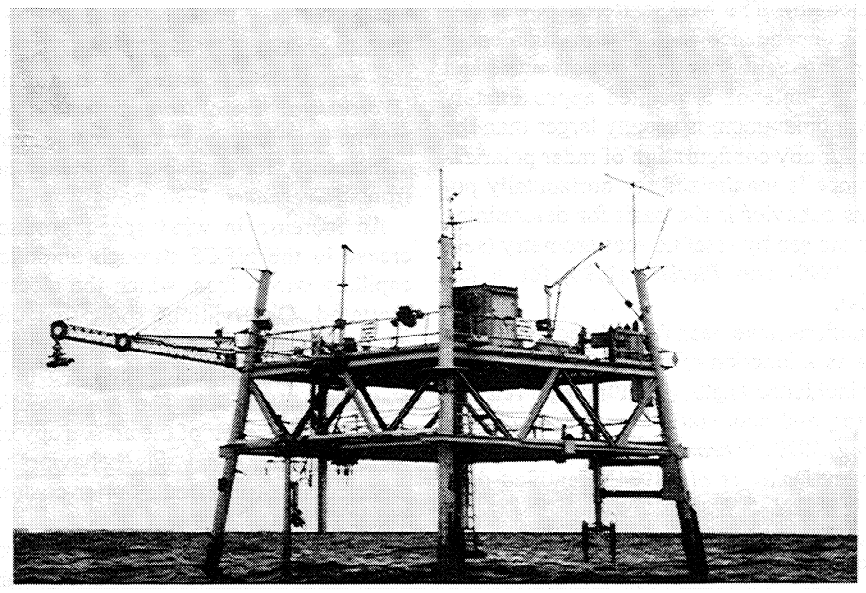

Figure 2. Photograph of the CCIW tower configured for WAVES '87. The 14.0 GHz (Ku band) radar is extended from a boom facing southwest. Wind and wind stress measurements are obtained from a bivane anemometer on the central mast, 11.5 m above the water surface.

Table 1. Summary of Environmental Conditions

Parameter	Value
Air Temperature, °C	−10–16.6
Water temperature, °C	3.8–7.0
Air-water temperature difference, °C	−13.8–9.6
Relative humidity, %	40–100
Wind speed, m/s	<15
Wind direction	All directions except 90°–180°
Significant wave height, m	<3

we then show that parameterizing the NRCS on wind stress removes much of its dependence on atmospheric stratification. Section 6 addresses the azimuthal angular dependence of the NRCS. Finally, section 7 summarizes our results.

2. Experimental Details

2.1. The Site

The data analyzed in this study were acquired between November 11 and December 12, 1987, from an instrumented, bottom-mounted tower at the western end of Lake Ontario, near Hamilton, Ontario (Figure 1). The tower is positioned 1.1 km offshore at a freshwater site with 12-m depth, small residual surface currents, and fetch ranging from 1 to 300 km. The tower is of a bilevel design (Figure 2) with an upper deck (100 m^2) constructed of open grating to minimize flow distortion, and a lower walkway 4 m above the water surface. At the center of the upper deck is a mast on which the meteorological sensors are mounted; at the foot of the mast is the data acquisition system housing. Power is supplied to the tower from an onshore source via an underwater cable. *Donelan et al.* [1985] provide full details of the tower and local geography.

Due to the location of the study site in Lake Ontario, the ranges of some environmental parameters which influence the NRCS differ somewhat from those over the open ocean. The wind direction is primarily from the west, i.e., from the short-fetch direction. Unlike the open ocean, the site exhibits a wide range of atmospheric stratification, which is correlated with the fetch. The most unstable conditions occur when winds are from the north to northwest so that cold polar air flows over the lake. Near-neutral conditions are measured when the wind is from the north to northeast so that the site is dominated by marine air. The most stable situations occur when the wind is from the south to southwest, bringing warmer air over the water. Furthermore, Lake Ontario is a freshwater lake. At the microwave frequencies used in the experiment, however, the dielectric constants of fresh and salt water are indistinguishable, so the measured NRCS should adequately represent ocean conditions [*Klein and Swift*, 1977].

WAVE LENGTH	BRAGG WAVE 20 40 60 80	HPOL or VPOL	DYNAMIC RANGE
2.14	3.1 1.6 1.2 1.1 all cm	dual	72 dB

AZIMUTH ANGLE VARIATION

Ku-band scatterometer sweeps through approx 300 deg every ten minutes, from 95 through 0 to 30 deg T.

INCIDENCE ANGLE VARIATIONS

Recording Period	Angle	Comment
5 minutes	0	Specular reflections
10 minutes	10	"Calibration" angle
		Little wind speed dependence
20 minutes	20	Spec/diffuse (soft) boundary
20 minutes	40	Diffuse (Bragg) scatter
20 minutes	60	Diff/grazing (soft) boundary
20 minutes	80	Grazing angle scattering
_____		(system noise evaluation)
95 min continuous run		

Figure 3. Characteristics of the 14.0-GHz microwave system.

Environmental conditions encountered at the tower during the experiment are summarized in Table 1. The first and fourth week of data collection were associated with stably stratified atmospheric conditions (positive air-water temperature differences), while the middle 2 weeks had predominantly unstable stratification. The relative humidity was quite variable, ranging from 40 to 100%, which included several periods of heavy rain. Only moderate wind speeds were measured. A feature to note is that there were no winds from the southeast quadrant of the compass (90° to 180°) during the experiment. Finally, the water temperature range was only about 4°C, too small to perform a parametric analysis of water temperature effects on the NRCS.

2.2. The Microwave Scatterometer

A dual-polarized, continuous wave, coherent, Ku band (14 GHz) microwave system, supplied by the Naval Research Laboratory, was used in the experiment. The system design was the same as that described by *Plant et al.* [1994] except that two horns were used as receiving antennas. The effective two-way beam widths of the system were 6.24° and 7.33°, with the larger beam width being vertical for VV polarization and horizontal for HH. This implies a far-field range for the system of about 6.1 m. The system put out a reference voltage which was used to normalize the return signal for calibration. The calibration procedure was the same as that described by *Plant et al.* [1994]. The system was calibrated against both spheres and corner reflectors before and after the experiment. Because only 48 data communication channels were available to telemeter data from the tower, only the amplitude-modulated signal from the scatterometer was retained. This signal is proportional to the field received by the antenna averaged over 0.6 ms. Thus upon squaring and calibration, the signal provides the NRCS as desired [*Colton*, 1989], but it does not allow measurement of surface velocities as can be obtained through analysis of Doppler frequency shifts in the frequency-modulated signal. Throughout this experiment, horizontally and vertically polarized signals were obtained simultaneously.

The scatterometer was mounted on an antenna rotator at the end of a 7.6-m boom pointing away from the tower, and 7.6 m above the water surface (Figure 2). The rotator varied the azimuth angle of the scatterometer in a windshield wiper fashion, omitting those angles at which the beam intersected the tower. One 300° sweep was made every 10 min by stepping 5° in azimuth approximately every 10 s. The incidence angle of the antenna was also varied in the sequence summarized in Figure 3 in order to cover the range of incidence angles from 0° to 80°.

2.3. Environmental Sensors

A Gill-type bivane anemometer (R. M. Young Co., 1974), mounted on the tower mast at 11.5 m (Figure 2) was used to measure wind speed, wind direction, and momentum flux. The wind speed sensor is a four-blade polystyrene propeller with a 1-m distance constant (wind passage for 63% recovery of a step change in speed), threshold speed of about 0.2 m/s, and maximum recoverable velocity of 31 m/s. The delay distance of the vane (wind passage for a 50% recovery from a step change in direction) is 1 m, and its damped natural wavelength (distance in which directional oscillations are reduced by $1/e$) is 5.8 m.

The air temperature thermistor, also mounted at 11.5 m, had a time constant of 0.2 s and was shielded to minimize direct solar warming. The relative humidity sensor (a thin film capacitor) was mounted beneath a plate at the top of the mast on which the base of the anemometer rests. The response time of the fast response sensor element is less than 1 s at 20°C, with an accuracy better than ±3%. The water surface temperature sensor was contained in a modified "bucket," which was fixed just beneath the water surface against one of the tower legs and measured a temperature corresponding to the upper 10 cm of water. Calibration of the sensors was performed in the laboratory before and after the experiment (see *Tsanis and Donelan* [1987] for more details.)

2.4. Data Acquisition and Processing

All sensors were sampled and recorded in 95-min (nominal) data records. The 48-channel, analog data were digitized at 20 Hz on the tower and transmitted to a trailer onshore, where they were automatically received by a microcomputer. The raw voltages were converted to first-order geophysical variables (e.g., wind speed and air and water temperatures) using the laboratory calibration equations. One-minute running mean averages of the geophysical variables, evaluated every 10 s, as well as 10-s averages, were computed for temporal collocation with the rotating scatterometer.

The NRCS was computed for each 10-s azimuth bin, excluding about 10 points at the beginning and end of the antenna movement to guarantee accuracy in the azimuth angle assignment. Thus each average NRCS value was computed from about 180 samples taken 50 ms apart. Since Ku band Doppler widths are typically of the order of 100 Hz, these samples should be uncorrelated. The absolute cross-section values were obtained via the reference voltages from an internal calibration cycle at the beginning of each run and system noise levels from low-wind-speed, 80° incidence angle data. Normalization was accomplished using an illuminated area given by

$$A = \frac{\pi}{4} \Phi^2 R^2 / \cos\ \theta \tag{1}$$

where R is range to the surface, θ is incidence angle, and Φ is the one-way, full, half power beam width of the antennas.

Initial comparisons of the measured NRCS with scatterometer model function predictions as a function of incidence angle showed a positive 1- to 2-dB bias between the measured and predicted values at all incidence angles. Before attributing erroneous physical meaning to these biases, a further antenna pattern correction was applied to the NRCS data using the 10° incidence angle data. The 10° incidence angle data were used as an external "field" calibration point because they showed little dependence on either wind speed or wind direction for the environmental conditions encountered during the experiment. This calibration point may be more representative of the true calibration, since the radar is designed to detect Doppler shifts in the radar returns induced by the movement of the sea surface. This situation is only simulated in the laboratory calibration procedure through the use of an oscillating or rotating sphere.

It was presupposed that the tower radar cross sections at 10° may be higher than the corresponding predictions from the model functions which were tuned to airplane or satellite scatterometers, since the tower radar antenna has a beam

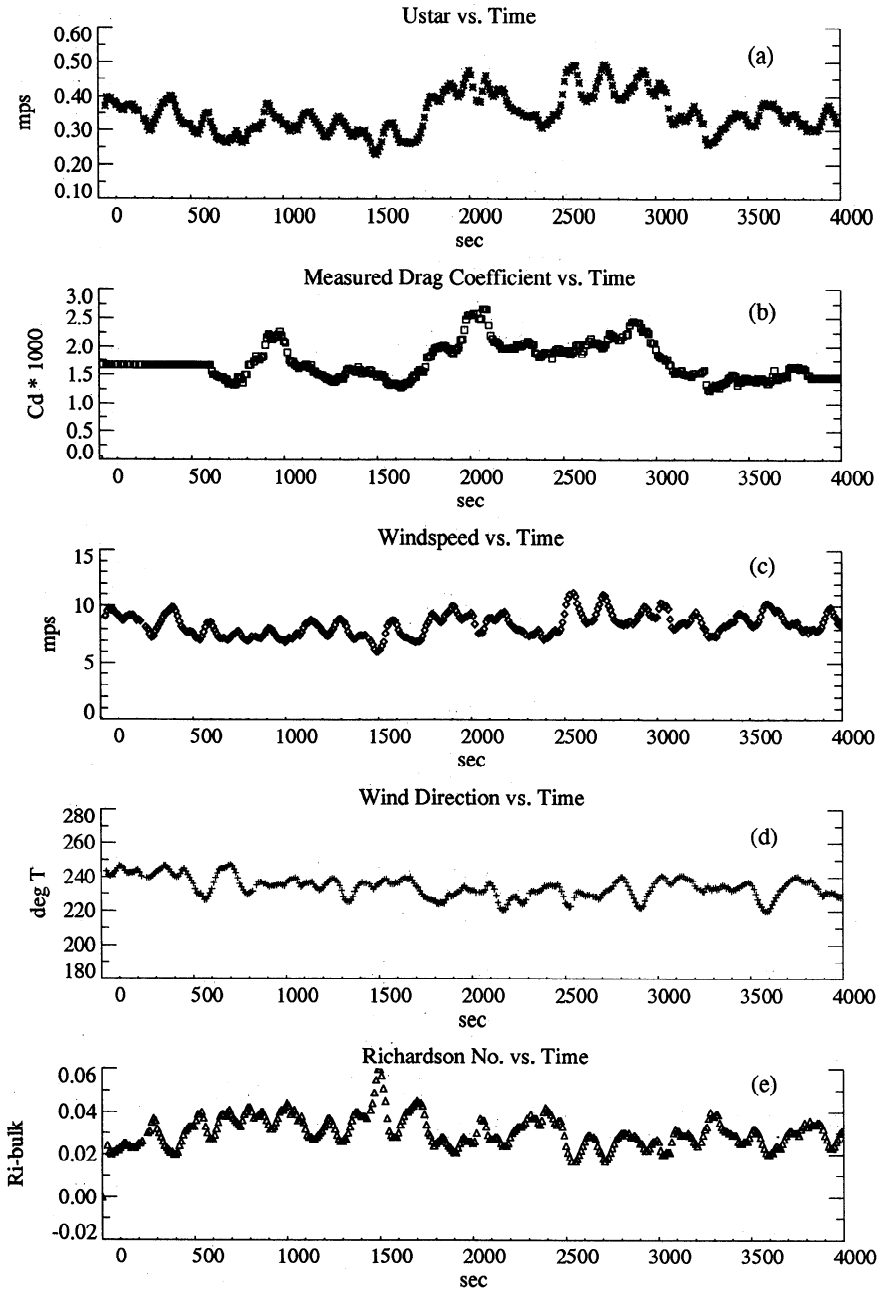

Figure 4. Wind and stability parameters as a function of time: (a) friction velocity in meters per second (mps), (b) drag coefficient, (c) wind speed, (d) wind direction, and (e) bulk Richardson number (data run 49, November 13, 1987, 1725 UT).

width of nearly 7° as compared with 1° or less for the higher-altitude scatterometers. To estimate the offset that would arise from the higher beam width, Seasat scatterometer model function predictions (SASS1 [*Schroeder et al.*, 1982] and SASS2 [*Wentz et al.*, 1984]) at 10° (averaged over all azimuth angles from 3 to 11 m/s) were "smeared" over a 7° beam width by assuming a Gaussian antenna pattern for the tower radar. The SASS1 and SASS2 model functions were chosen for this calibration because they were purely statistical fits of data from an aircraft scatterometer (1.5° beam width) and the Seasat scatterometer (0.5° beam width).

For SASS1 the averaged 10° value was 7.73 dB, or 0.73 dB higher than that obtained from the aircraft scatterometer. Similarly, the averaged 10° value was 7.44 dB for the SASS2 model, or about 1.1 dB higher than the satellite measurements. Therefore about 1 dB of the bias in the tower data was attributed to the wider beam width of the tower radar and was subsequently subtracted from all of the data plots to allow better comparison to existing model functions. With this beam width correction, the tower radar measurements at 10° incidence angle are within 1 dB of the values predicted by the Sesat scatterometer model functions.

The final data set included the Ku band (10 sec) NRCS at both HH and VV polarizations, wind speed, air and water temperatures, integrated wave spectral parameters and directional wave spectra (not discussed here), nondimensional numbers descriptive of overall environmental conditions

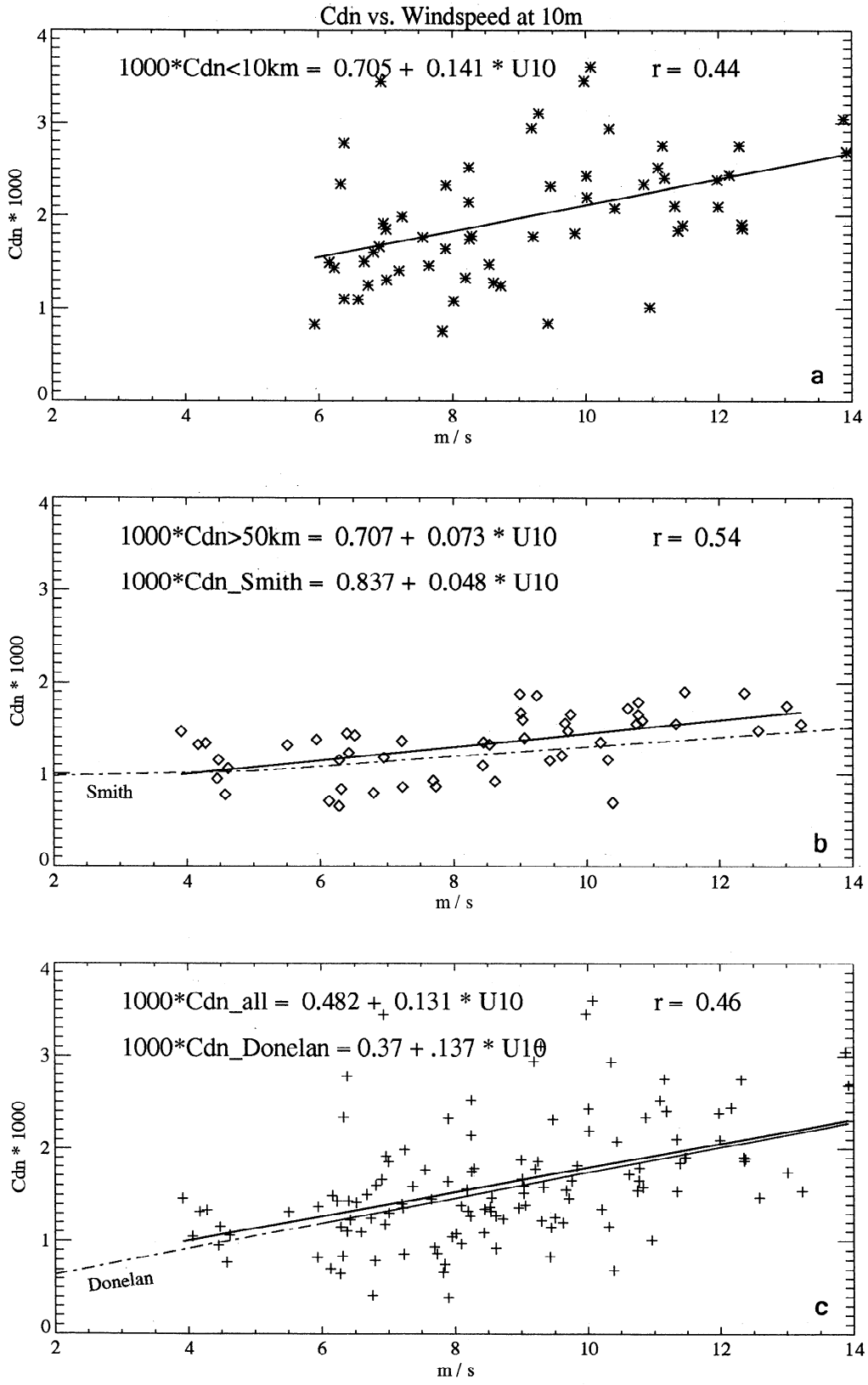

Figure 5. Neutral drag coefficient as a function of wind speed at 10 m for (a) short (<10 km), (b) long (>50 km), and (c) all fetch directions. For these plots, z/L was limited to -0.38 to 0.12.

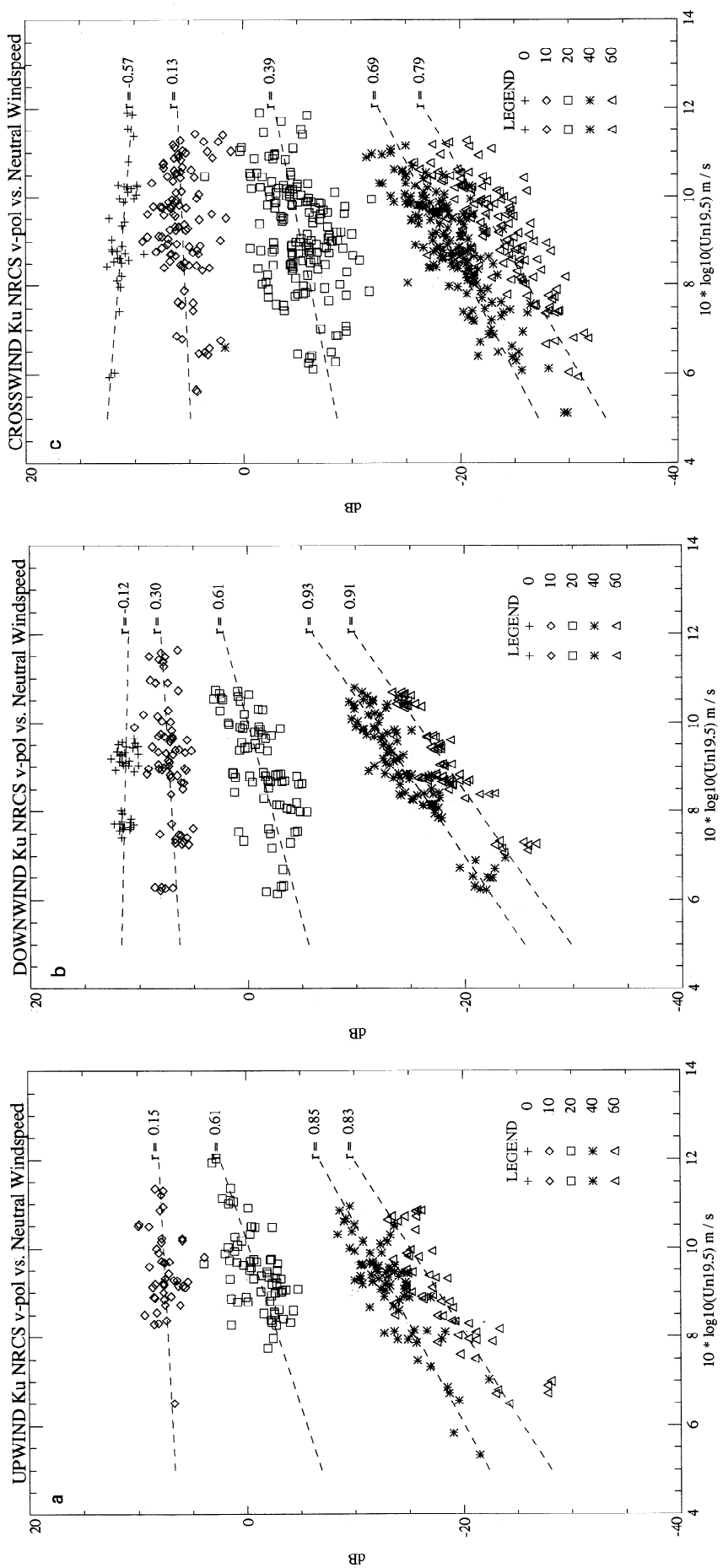

Figure 6. (a) Upwind, (b) downwind, and (c) cross-wind Ku band vertically polarized NRCS versus neutral wind speed at 19.5 m for multiple incidence angles for $-0.38 < z/L < 0.12$. The points are within 5° of the specified direction. In these plots a 1.0-dB beam width error was subtracted from the NRCS. Dashed lines are best fit linear regressions.

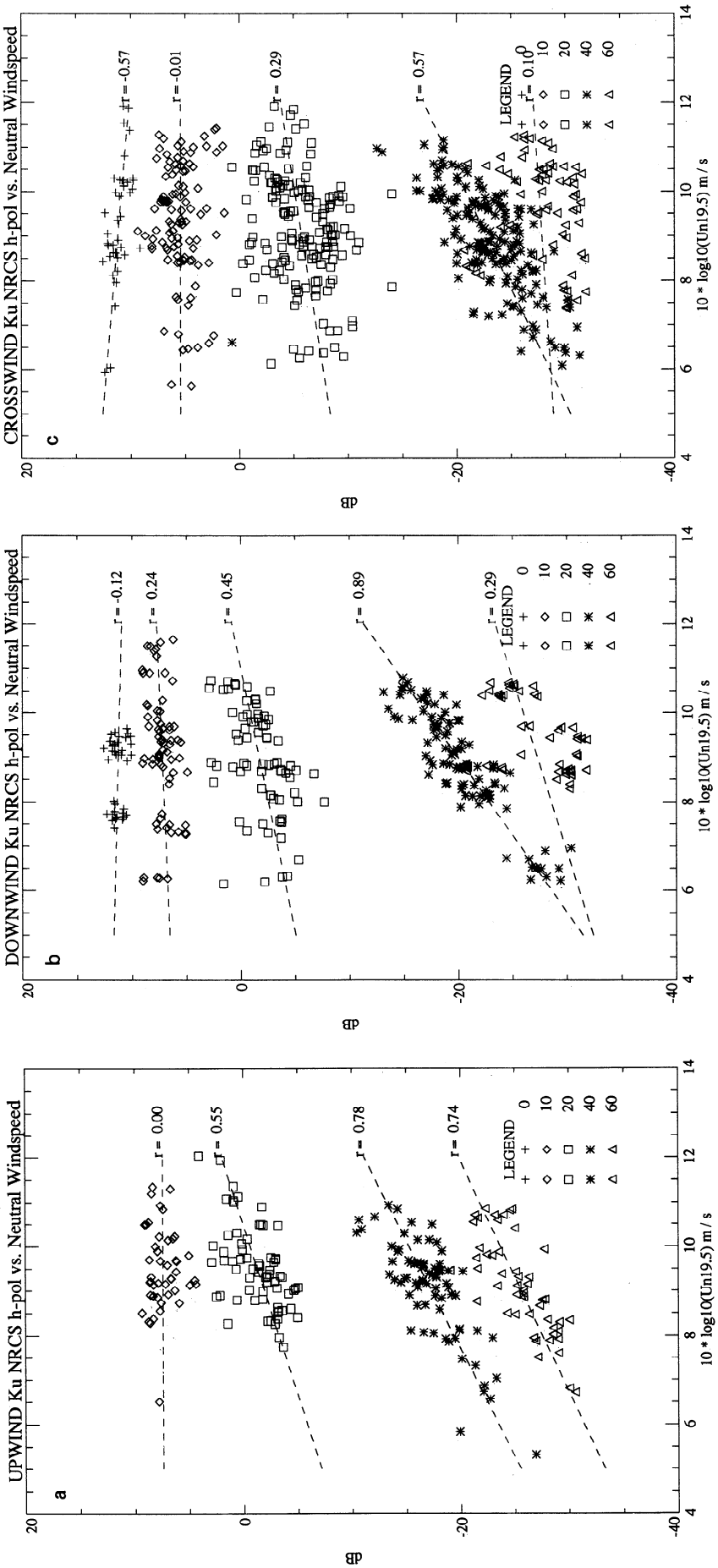

Figure 7. (a) Upwind, (b) downwind, and (c) cross-wind Ku band horizontally polarized NRCS versus neutral wind speed at 19.5 m for multiple incidence angles for $-0.38 < z/L < 0.12$. The points are within 5° of the specified direction. In these plots a 1.0-dB beam width error was subtracted from the NRCS. Dashed lines are best fit linear regressions.

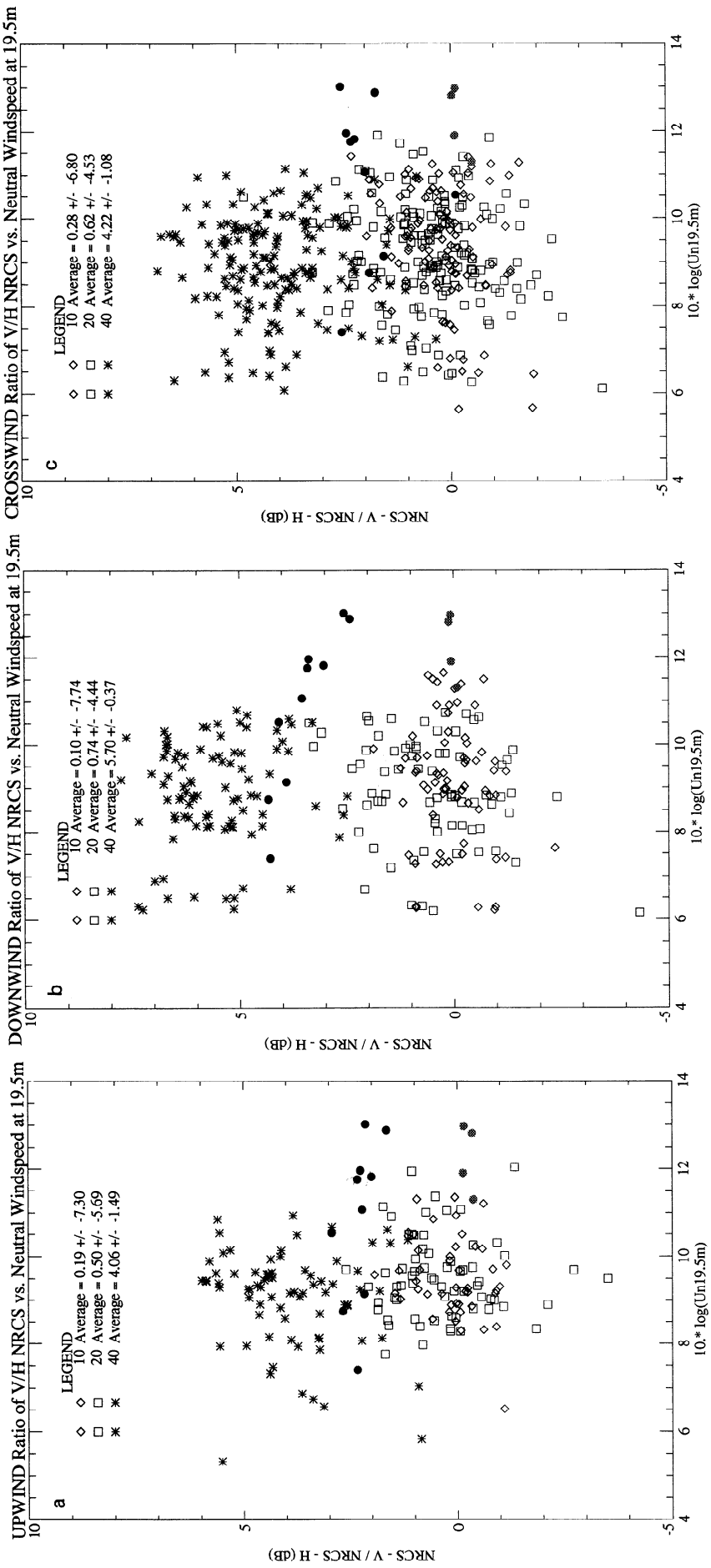

Figure 8. NRCS (a) upwind, (b) downwind, and (c) cross-wind polarization ratios (V-pol/H-pol) as a function of neutral wind speed at 19.5 m for multiple incidence angles. RADSCAT data are shown as shaded circles (20°) and solid circles (40°).

Table 2. Ku Band NRCS Parametric Dependence on $U_N(19.5)$: Comparison of Lake Measurements With AAFE RADSCAT Data

Angle, deg	Vertical Polarization				Horizontal Polarization			
	Lake		Ocean		Lake		Ocean	
	G	H	G	H	G	H	G	H
				Upwind				
0	...	...	1.45	−0.46	...	...	1.40	−0.36
10	0.57	0.20	0.50	0.0	0.74	0.0	0.55	0.0
20	−1.35	1.33	−1.40	1.05	−1.37	1.30	−1.30	1.00
40	−3.35	2.23	−3.20	1.77	−3.58	2.06	−3.55	1.98
60	−4.11	2.60	...	...	−4.29	1.92	...	...
				Downwind				
0	1.22	−0.10	1.45	−0.46	1.22	−0.10	1.35	−0.36
10	0.51	0.24	0.60	0.0	0.57	0.17	0.60	0.0
20	−1.12	1.11	−1.30	0.98	−0.92	0.84	−1.30	0.94
40	−3.94	2.77	−3.10	1.62	−4.59	2.88	−3.75	1.97
60	−4.40	2.84	...	...	−3.88	1.28	...	...
				Cross Wind				
0	1.43	−0.35	1.50	−0.46	1.43	−0.35	1.35	−0.36
10	0.41	0.16	0.60	0.0	0.55	−0.01	0.60	0.0
20	−1.27	0.81	−1.50	0.98	−1.16	0.65	−1.35	0.75
40	−3.77	2.10	−3.30	1.52	−4.01	1.93	−3.60	1.46
60	−4.53	2.38	...	...	...	...	...	...

(defined later), neutral wind speed at several heights, wind stress, and measured and neutral drag coefficients.

3. Computation of the Wind Stress and Neutral Wind Speed

When relating the NRCS to environmental measurements, one must consider the local (microscale) problem of momentum transfer to waves which are small compared with the longest gravity waves present in the larger, spatially averaged (macroscale) wave field. Momentum transfer from wind to waves may be quantified by the friction velocity u_* in the growth rates of the short waves. Therefore in scatterometer studies the wind stress should be evaluated at timescales comparable to the timescale of the Bragg-scattering waves, i.e., a timescale of seconds.

On the other hand, the macroscale wave field exerts a drag on the wind which modulates the wind stress. The stress is supported by a range of wavenumbers, whereas the scatterometer is wavenumber selective (within a small band about the Bragg wavenumber). Therefore a different timescale is needed to quantify sea state effects on the wind stress. With the assumption of horizontal homogeneity in the surface wave field and ignoring the microscale, the typical approach to this problem has been to determine an overall roughness length z_0 dependent on the drag coefficient, which parameterizes the wave drag on the wind. Wave state and stratification have time and space scales much larger than the microscale; therefore the drag coefficient has inherently longer timescales, of the order of minutes, and larger spatial scales, of the order of kilometers.

To separate the microscale effects from the macroscale, we assume that the friction velocity is proportional to a long-term drag coefficient C_D and short-term wind speed, i.e.

$$u_*^2|_{O(\text{sec})} = C_D|_{O(\text{min})} U^2(z)|_{O(\text{sec})} \tag{2}$$

where U_z is the wind speed at height z. In this manner, the observed rapid changes in cross section with wind speed are accounted for by using a short-timescale wind speed to compute the wind stress. The variation of stress over longer timescales is taken into account by using a long-term drag coefficient. The procedure is to compute u_* and the mean wind at measurement height, $U(z)$, from the wind components over the long timescale and then to form the ratio of u_*^2 to $U(z)^2$ to obtain the long-term drag coefficient. This drag coefficient is used in (1) with the short-term wind speed average to compute a short-term stress.

The stress is estimated directly by forming the covariance between the fluctuating horizontal (u', v') and vertical (w') components of the wind and applying Reynold's rules of averaging [*Panofsky and Dutton*, 1974, p. 88]. The stress vector $\boldsymbol{\tau}$ is then

$$\boldsymbol{\tau} = (-\overline{u'w'}\hat{\mathbf{i}} - \overline{v'w'}\hat{\mathbf{j}}) \tag{3}$$

where the first term on the right is the longitudinal stress and the second is the lateral stress. The friction velocity squared is given by the magnitude of the stress divided by air density ρ,

$$u_*^2|_{O(\text{sec})} = |\boldsymbol{\tau}/\rho| = [(\overline{u'w'})^2 + (\overline{v'w'})^2]^{1/2} \tag{4}$$

and the stress direction α, relative to the wind direction, is given by

$$\alpha = \tan^{-1}(\overline{v'w'}/\overline{u'w'}) \tag{5}$$

(α is positive when $\boldsymbol{\tau}$ is to the right of the wind vector).

The turbulent fluxes and covariances were measured using an averaging time of about 20 min, which is approximately 4 times the period of the largest eddies in the boundary layer [*Geernaert*, 1988], and also still within the spectral gap between the synoptic and turbulent peaks in the wind speed spectrum [*Pierson*, 1983]. The choice of averaging time for

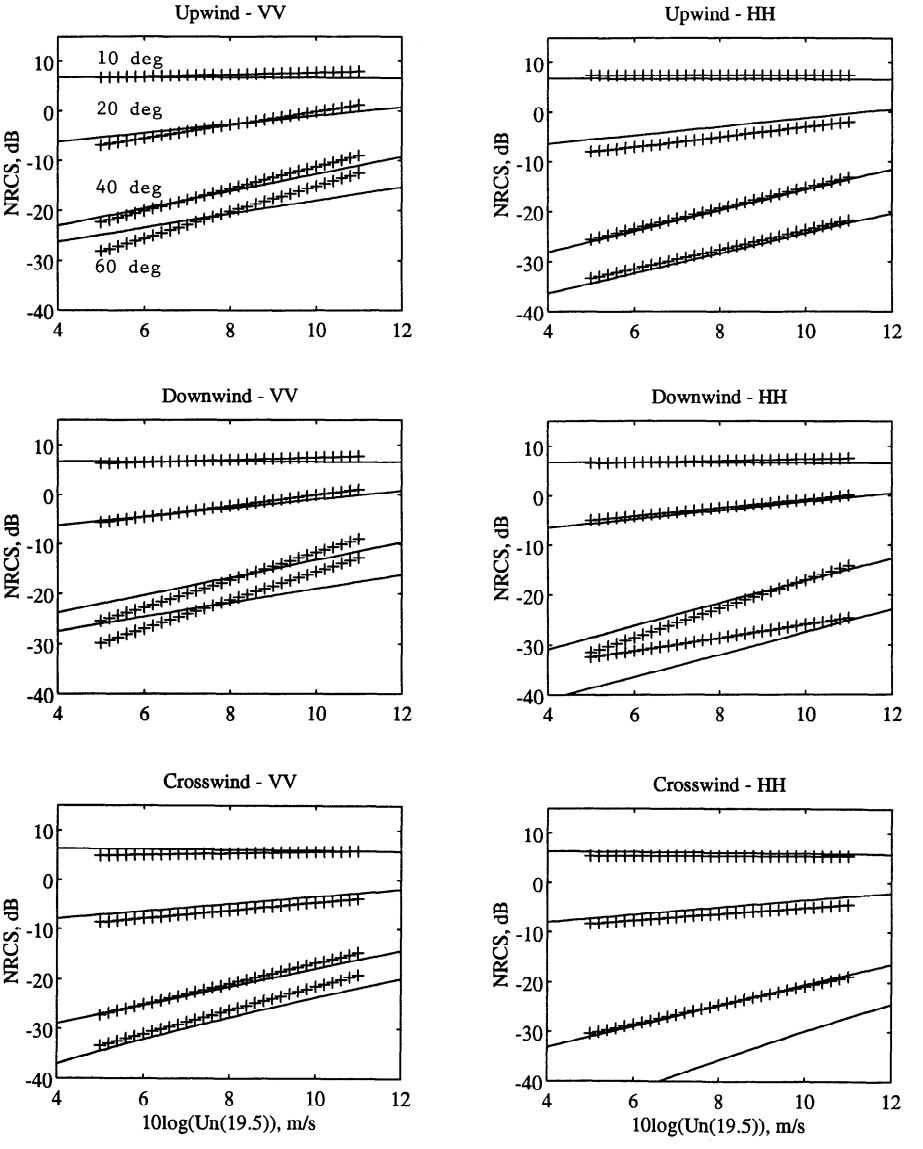

Figure 9. NRCS (pluses) and SASS II model function (solid lines) versus $U_N(19.5)$ measured on the lake.

the wind stress also determines the accuracy of the computed stress. For neutral conditions at a measurement height z, wind speed U, and specified accuracy ε, *Wyngaard* [1973] shows that the averaging time T is given by

$$T_{u'w'} = 20z/\varepsilon^2 U \tag{6}$$

With $T_{u'w'} = 20$ min, $z = 11.5$ m, and a typical U of 7.5 m/s, the accuracy of the covariance computed for illustration is ±16%. Accuracy will rapidly decrease with decreasing wind speed.

For our data set we used a moving 20-min average evaluated every 10 s in order to maintain continuity of the drag coefficient between independent 20-min records and to allow correlation of the computed drag coefficient with a particular 1-min (microscale) wind speed. This averaging method allows each Ku band azimuth bin to be assigned a unique stress value.

Using the 20-min averaged u_* and wind speed values, a 20-min drag coefficient and corresponding 1-min stresses were computed. These, along with wind direction and bulk Richardson number, are shown in Figure 4, where stress is given in terms of u^*. In this example the drag coefficient has a mean value of about 0.0018 and no trend, but significant temporal variations, which span a range of values from 0.0012 to 0.0026. The short-term friction velocity has the overall character of the longer-term 20-min drag coefficient, but it also incorporates the effect of the short-timescale variations in the wind speed.

We plot the 20-min running mean bulk Richardson number Ri_B, a measure of atmospheric stability, in Figure 4e. This parameter is based on local scaling and is defined as

$$Ri_B = \frac{gz(T_{V\mathrm{Air}} - T_{V\mathrm{Sea}})}{T_{V\mathrm{Air}}U^2} \tag{7}$$

where g is the gravitational acceleration constant; z is measurement height, and T_V is the virtual air or sea temperature (in degrees Kelvin). The atmosphere was stably strat-

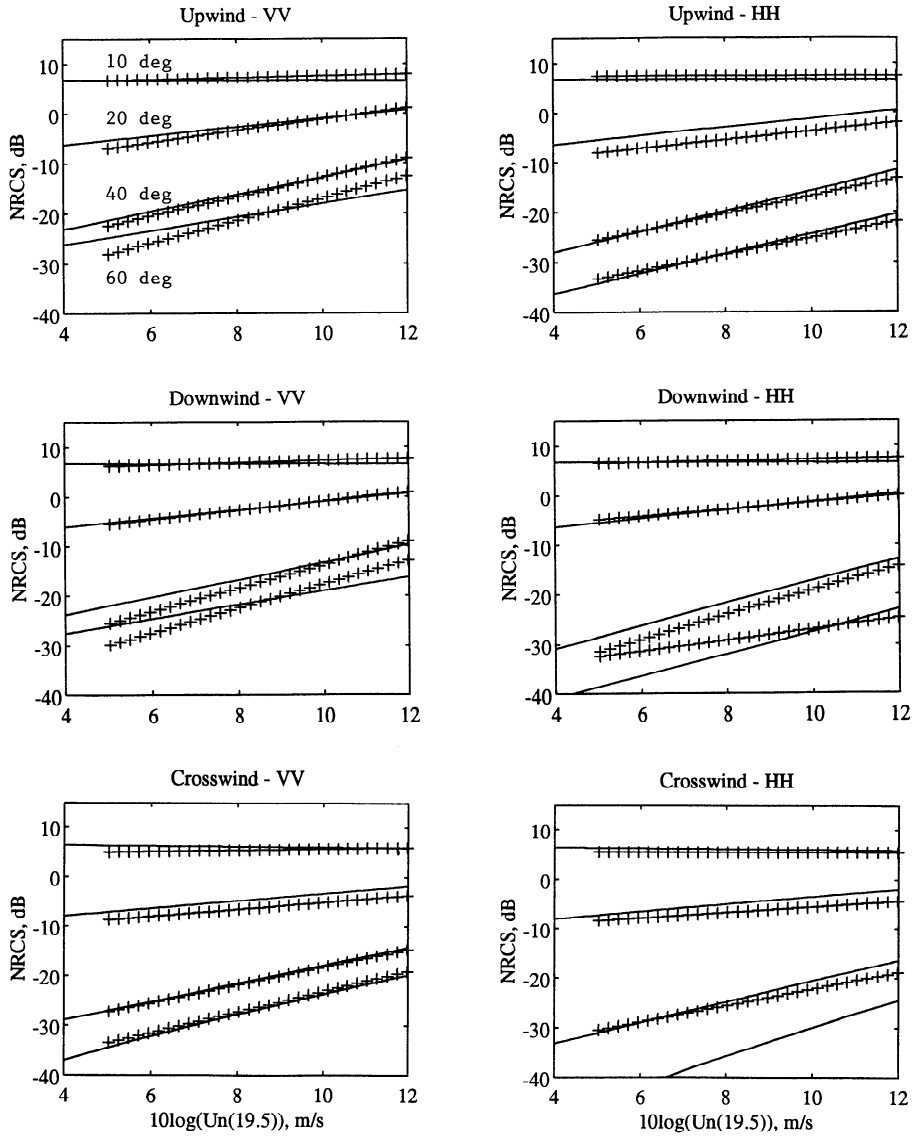

Figure 10. Same as Figure 8, but with regression lines plotted against the "equivalent" ocean $U_N(19.5)$, which produces the same friction velocity as the lake winds.

ified for this data run, as is indicated by the positive value of the Richardson number.

To obtain the neutral wind speed, we used the measured 20-min drag coefficient and obtained its neutral value using the following relation:

$$C_{DN} = [C_D^{-1/2} + \Psi/\kappa]^{-2} \tag{8}$$

where κ is the von Kármán constant (taken as 0.4) and $\Psi(z/L)$ is a stability correction to the wind profile. The functional form of $\Psi(z/L)$ is the same as those used by *Geernaert et al.* [1988]. The relation between Ri_B and Monin-Obukhov scaling and stability was obtained from *Donelan et al.* [1974]:

$$\begin{aligned} z/L &= 7.6Ri_B \qquad Ri_B < 0 \\ z/L &= 6.0Ri_B \qquad Ri_B > 0 \end{aligned} \tag{9}$$

The 1-min neutral wind speed is given by

$$U_N(11.5 \text{ m}) = C_{DN}^{-1/2} u_* \tag{10}$$

where u_* in (10) is the 1-min friction velocity. At any other level z,

$$U_N(z) = U_N(11.5) + u_*/\kappa \ \ln (z/11.5) \tag{11}$$

For example, the neutral wind speed at 11.5 m is systematically around 2% larger than the 10-m neutral wind speed.

We have employed the above measurement techniques and equations to compute neutral drag coefficients during our experiments for the conditions when the wind direction produced short fetches and when it produced long fetches. Fetches longer than 50 km could be produced only when the wind direction was between 44° and 98°, so we take these angles as defining long-fetch data. Similarly, fetches less than 10 km occurred when the wind direction was greater than 123° and less than 6°. Figure 5 shows the measured C_{DN}

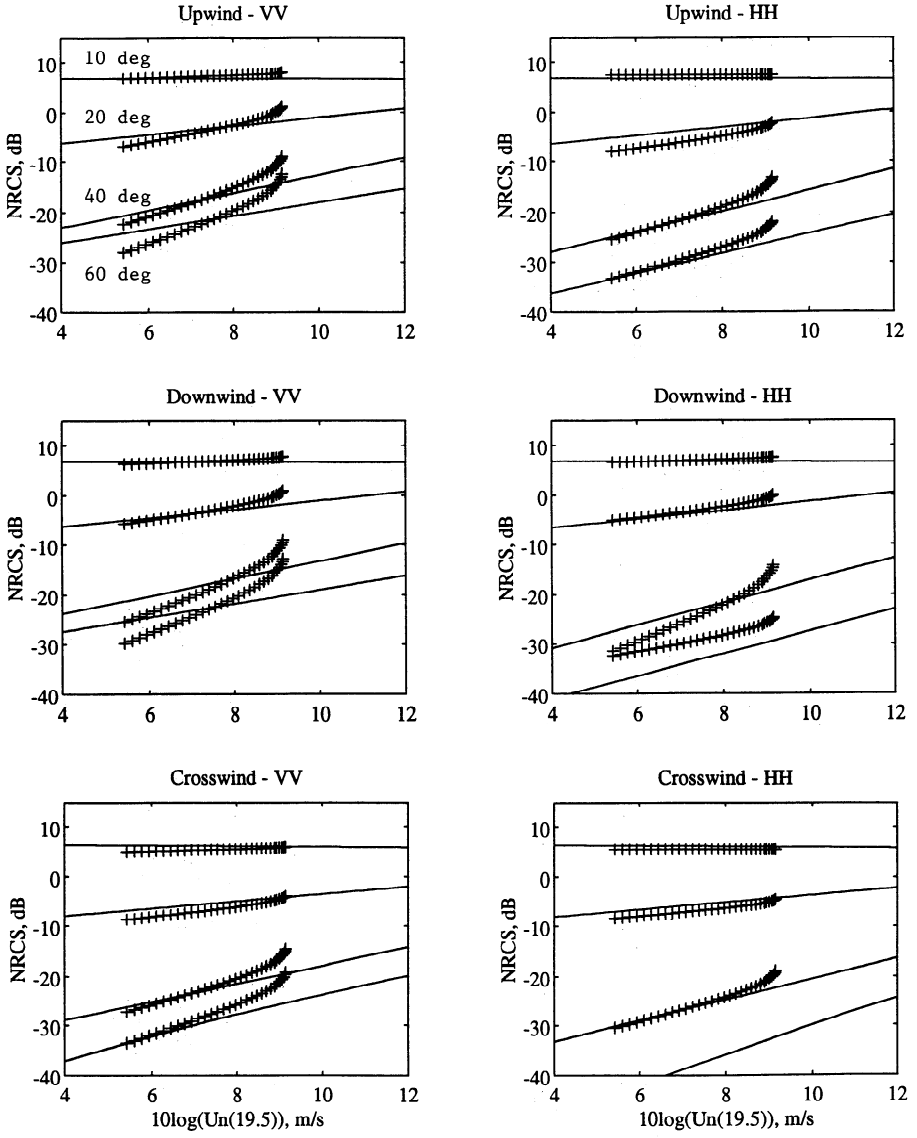

Figure 11. Same as Figure 8, but with lake regression lines plotted against the "equivalent" ocean $U_N(19.5)$, which produces the same wind speed 2 cm above mean water level as the lake winds.

for these two cases along with the best fit lines to the two sets of data in the least-squares sense. These lines are defined by the following equations:

$$C_{DN} = 0.001(0.705 + 0.141U(10\text{ m})) \qquad \text{fetch} < 10\text{ km} \tag{12}$$

$$C_{DN} = 0.001(0.707 + 0.073U(10\text{ m})) \qquad \text{fetch} > 50\text{ km} \tag{13}$$

Smith [1988] has given the best fit C_{DN} for winds on the ocean to be

$$C_{DN} = 0.001(0.837 + 0.048U(10\text{ m})) \tag{14}$$

Note that C_{DN} on the lake for short fetches has a slope about 3 times that of the oceanic drag coefficient. For the long fetches, however, the lake drag coefficient has a slope only 1.5 times greater than the ocean data.

Donelan et al. [1982] suggested that the larger C_{DN} values observed on the lake were due to the younger, steeper waves associated with short fetch. Over a range $-0.38 < z/L < 0.12$, their measured C_{DN} was given as

$$C_{DN} = 0.001(0.37 + 0.137U(10\text{ m})) \tag{15}$$

In the present measurements, over the same z/L range and all fetches, we obtained

$$C_{DN} = 0.001(0.48 + .131U(10\text{ m})) \tag{16}$$

We will return to the fetch-dependent behavior of C_{DN} in the next section, where we will use it to investigate the manner in which the NRCS depends on wind.

4. NRCS Dependence on Wind Speed Parameters

After obtaining the neutral wind speed at 19.5 m above the surface of the lake from (11) using our measured values of u_*

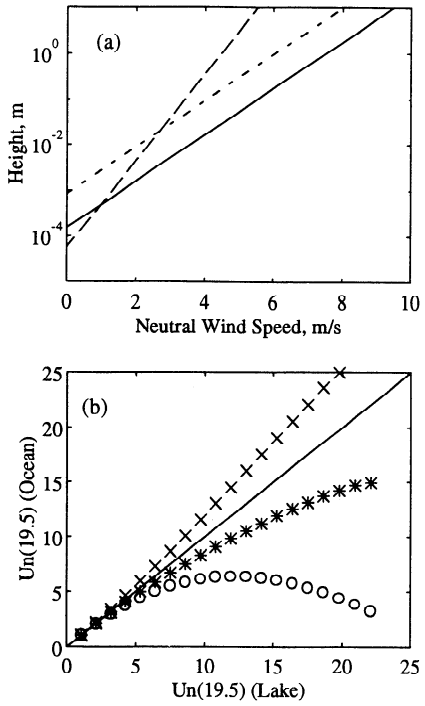

Figure 12. Comparison of lake and ocean winds. (a) Solid line is a wind profile from the lake. Dotted line is wind profile on the ocean which has the same friction velocity as the lake. Dashed line is wind profile on the ocean which produces the same wind speed 2 cm above mean water level as the lake. (b) Pluses indicate the ocean $U_N(19.5)$, which produces the same u_* as the lake $U_N(19.5)$. Asterisks and open circles show the ocean $U_N(19.5)$ which produces the same $U_N(z^*)$ as the lake $U_N(19.5)$ for $z^* = 0.15$ m and 0.02 m, respectively. Line of equal agreement is solid.

and $U_N(11.5)$, we determined the dependence of the NRCS for selected azimuth angles on $U_N(19.5)$. The NRCS data were grouped into azimuth angle ranges corresponding to upwind, downwind, and cross wind with an allowance of 5° about each prescribed direction. Data corresponding to friction velocities less than 0.12 m/s were omitted from the data set because they were too low for the bivane to measure accurately. Similarly, points corresponding to relative humidities above 90% were omitted, since they corresponded to rain with a high degree of probability. Finally two runs of questionable quality were omitted. One of these was of very short duration, while the other appeared to contain reflections from a solid object.

Plots of the resulting data set showing the NRCS in decibels versus 10(log $(U_N(19.5))$ where U_N is given in meters per second are presented in Figures 6 and 7 for incidence angles of 0°, 10°, 20°, 40°, and 60°. Also shown in these figures are the best fit linear regression lines for these log/log plots and the correlation coefficients for the various fits. Figure 8 shows the polarization ratios measured in this experiment along with those from *Jones et al.* [1977]. Note that the fetch has not been restricted in these figures. If we represent the NRCS in the manner of SASS1, the Seasat scatterometer algorithm, we have

$$\sigma^0 = 10(G + H \log (U_N(19.5)) \quad (17)$$

Values of G and H for our regression lines are given in Table 2 for the various fits.

Also shown in Table 2 are G and H values for ocean backscatter data collected by the NASA Advanced Applications Flight Experiment radiometer-scatterometer (AAFE RADSCAT) system [*Jones et al.*, 1977]. Comparison of the values of G and H for the present study on Lake Ontario with their counterparts for the ocean data shows that while G for the lake seems to be randomly distributed around the ocean value, H for the lake is generally higher than that for the ocean. In fact, this is always true at a 40° incidence angle. The higher values of H at this incidence angle are difficult to explain on the basis of instrumental errors and may indicate true differences in the behavior of the NRCS over the lake and ocean.

This possibility of a stronger wind speed dependence is further strengthened by Figure 9 where the regression lines for the lake data for 10°, 20°, 40°, and 60° incidence angles are plotted on the same graphs as the SASS2 model function [*Wentz et al.*, 1984]. Again, the slopes of the regression lines for the lake data are generally larger than those of the model function, which were derived from ocean NRCS values collected by Seasat. Note that the one conspicuous exception to this statement, downwind, HH-polarized NRCS values at 60°, is probably the most suspect of the lake regression lines, since the data used in deriving it are bunched between about 8 and 11 m/s (see Figure 7b).

In the plots of Figures 6–9 and the numbers of Table 2, the neutral wind speed at 19.5 m against which the NRCS values from the present study have been plotted are those that actually exist on the lake, i.e., wind speeds inferred from (11) using u^* and $U_N(11.5)$ as measured on the lake. The large values of H for the lake data may be interpreted to imply that this is not the proper wind parameter to hold constant when comparing lake and ocean data. In other words, the data indicate that $U_N(19.5)$ is not the wind parameter upon which the NRCS actually depends. This leads us to examine the possibility that another parameter of the wind should be held constant in comparisons of lake and ocean data.

Two possibilities have been suggested in the literature. Many authors have suggested that the NRCS depends on the friction velocity, or wind stress, rather than on the wind itself [*Durden and Vesecky*, 1985; *Plant*, 1986; *Weissman et al.*, 1990]. If this is true, then the proper comparison between lake and ocean NRCS values is at the same friction velocity rather than at the same $U_N(19.5)$. Alternatively, *Donelan and Pierson* [1987] have suggested that the NRCS responds to the wind speed very close to the surface; they chose a very small height equal to one-half the Bragg-resonant wavelength, or about 1 to 2 cm for Ku band. They interpreted this to mean the wind that would be present 1 to 2 cm above the mean surface if the logarithmic profile were extrapolated to levels below the crests of the surface waves. This suggestion may be generalized by holding the wind speed at an arbitrary height z^*, to be constant when comparing lake and ocean NRCS values. We now examine these two possible alternatives by computing "equivalent" $U_N(19.5)$ wind speeds in the sense that they produce the same friction velocity or $U_N(z^*)$ on the lake and on the ocean. The NRCS regression lines will then be plotted against these "equivalent" winds to see if the agreement between lake and ocean data is improved.

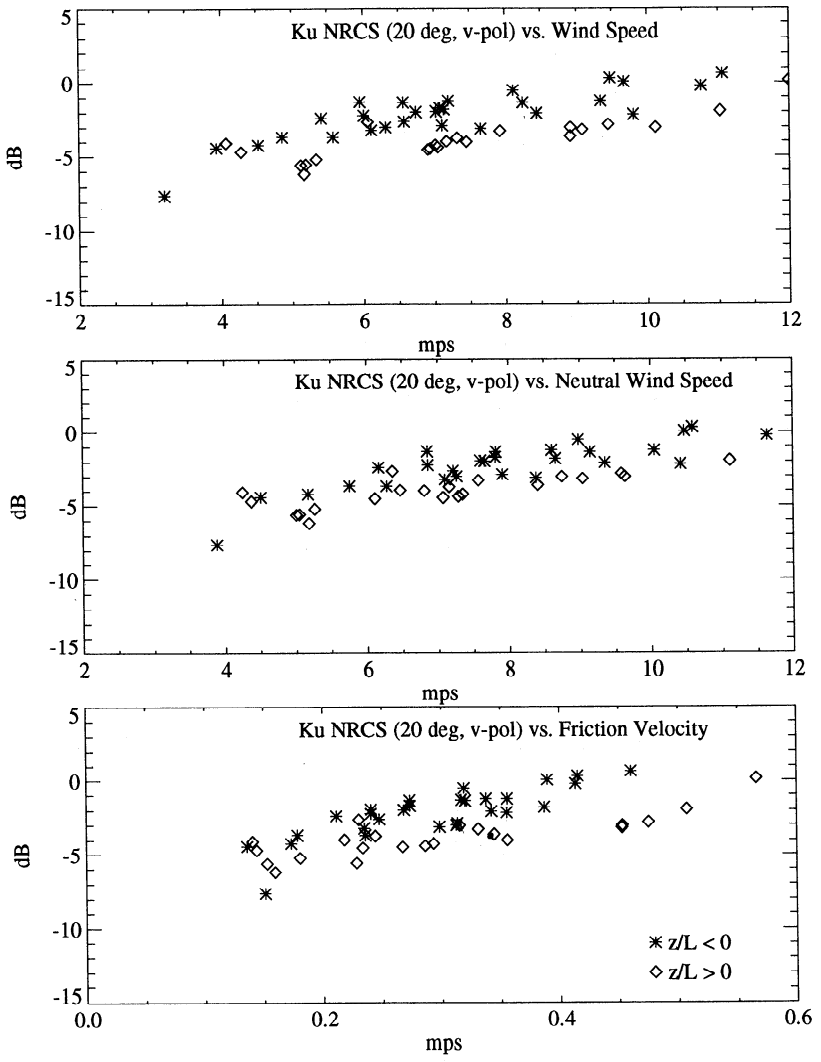

Figure 13. Azimuthally averaged, 20° incidence angle, vertically polarized Ku band NRCS as a function of measured wind speed, neutral wind speed, and friction velocity. Diamonds correspond to NRCS values where $z/L > 0$ (stably stratified atmosphere), whereas asterisks correspond to $z/L < 0$ (unstable).

We first derive an expression for the $U_N(19.5)$ which will produce the same u^* values on the lake and ocean. From (10), we have

$$U_{N\_Sea}(10) = \left[\frac{C_{DN\_Lake}}{C_{DN\_Sea}}\right]^{1/2} U_{N\_Lake}(10) \qquad (18)$$

where $U(10\text{ m})$ is used because the oceanic drag coefficient is typically regressed against wind speed at this height. Using this expression along with (11), (14), and (16), we may obtain a set of $U_{N\_Sea}(19.5)$ values which are equivalent to those used for the plots in Figure 9 in the sense that they are ocean winds which produce the same u^* as the lake winds used in Figure 9. We may therefore replot the regression curves for the lake against these new equivalent wind speeds for the ocean.

One problem is encountered in computing the equivalent wind speeds: the ocean drag coefficient given in (14) is specified in terms of ocean winds. Thus an iterative process is necessary in which lake winds are first used to obtain the ocean drag coefficient, the equivalent ocean wind is computed, and it is then used to reestimate C_{DN_Sea}. When C_{DN_Sea} stops changing, the process has converged, and equivalent ocean winds have been obtained. The result of plotting our lake regression lines against these equivalent winds is given in Figure 10. In most cases, the lake regression curves are now closer in slope to those obtained over the ocean.

Next consider the $U_N(19.5)$ on the ocean which produces the same $U_N(z^*)$ as on the lake. Using (11) to compute $U_N(z^*)$ on both the lake and ocean and setting them equal yields

$$U_{N\_Sea}(19.5) = \frac{u_{*\_Sea}}{\kappa}\left[\ln\left(\frac{19.5}{10}\right) + \kappa C_{DN\_Sea}\right] \qquad (19)$$

$$u_{*\_Sea} = \left[\frac{\ln(z^*/10) + \kappa C_{DN\_Lake}^{-1/2}}{\ln(z^*/10) + \kappa C_{DN\_Sea}^{-1/2}}\right] u_{*\_Lake} \qquad (20)$$

Using the iterative procedure with these equations, we related $U_{N\_Sea}(19.5)$ to $U_{N\_Lake}(19.5)$, assuming that $U_N(0.02\text{ m})$ is constant. When we plot the lake NRCS regression curves versus this new $U_{N\_Sea}(19.5)$, we obtain

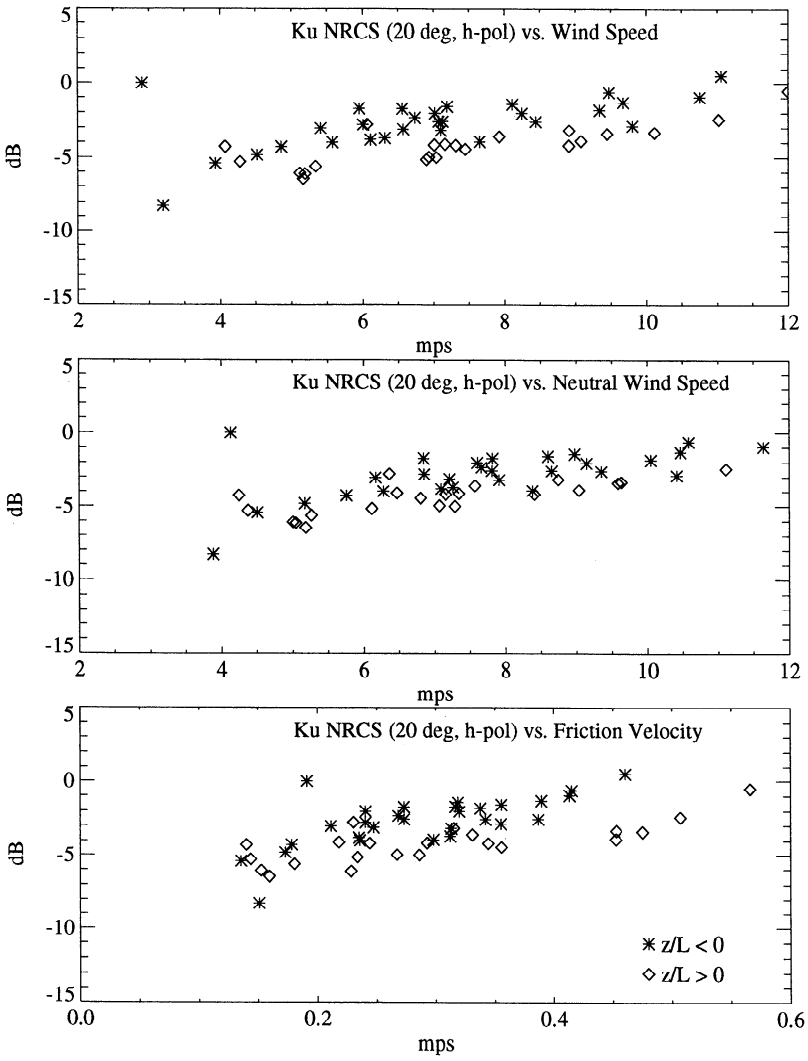

Figure 14. Azimuthally averaged, 20° incidence angle, horizontally polarized Ku band NRCS as a function of measured wind speed, neutral wind speed, and friction velocity. Diamonds correspond to NRCS values where $z/L > 0$ (stably stratified atmosphere), whereas asterisks correspond to $z/L < 0$ (unstable).

the curves shown in Figure 11. In this case, the slopes of the regression lines are even larger than in Figure 9. Indeed it is easy to show using (10) and (11) that this will always be the case as long as $z^* < 19.5$ m. As z^* decreases or as $U_{N\_Lake}(19.5)$ increases, the NRCS regression curves eventually become nonsense when plotted against $U_{N\_Sea}(19.5)$ because they double back on themselves producing double-valued cross-sections at a constant wind speed.

Figure 12 makes the reason for this behavior clear. Figure 12a shows wind speed profiles on the lake and on the ocean under the two different assumptions. As these figures show, $U_{N\_Sea}(z)$ differs from $U_{N\_Lake}(z)$ in a very different manner if the wind speed at $z = z^*$ is held constant (dashed line) than it does if u_* is held constant (dotted line). Figure 12b plots $U_{N\_Sea}(19.5)$ against $U_{N\_Lake}(19.5)$ for u_* constant (pluses) and for $U_N(z^*)$ constant when z^* is 0.02 m (circles) and 0.15 m (asterisks). The curvature of the constant $U_N(z^*)$ curve becomes more negative as z^* decreases and eventually yields two $U_{N\_Sea}(19.5)$ values for each $U_{N\_Lake}(19.5)$ value.

5. NRCS Dependence on Atmospheric Stratification

The results of section 4 suggest that u_* is the primary parameter upon which the NRCS depends. If this is true, then most dependence of the NRCS on atmospheric stability should be removed if u_* is held constant. To investigate whether this is indeed the case, we stratified our data set according to atmospheric stability as represented by z/L for the cases of constant $U(11.5)$, constant u_*, and constant $U_{N\_Lake}(19.5)$. This procedure was complicated by the fact mentioned earlier that on Lake Ontario, atmospheric stability and wind direction are highly correlated. Since the fetch depends on the wind direction, this implies a correlation between stability and dominant wave slope. Since it is known that the dominant wave slope influences the NRCS in stable situations, we attempted to analyze our data in a manner that would hold the wind direction relatively constant.

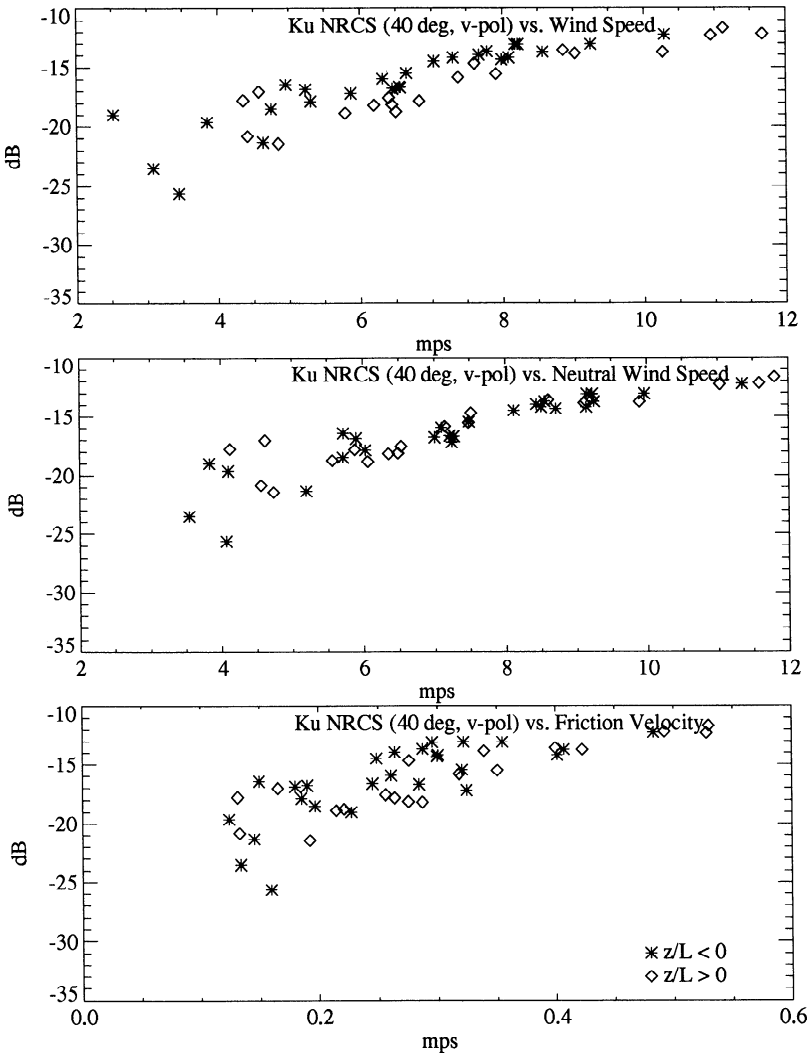

Figure 15. Azimuthally averaged, 40° incidence angle, vertically polarized Ku band NRCS as a function of measured wind speed, neutral wind speed, and friction velocity. Diamonds correspond to NRCS values where $z/L > 0$ (stably stratified atmosphere), whereas asterisks correspond to $z/L < 0$ (unstable).

Binning the data on wind direction quickly reduced the number of situations we were able to examine for stability effects. In order to increase the statistical significance of the data, we decided to investigate only the dependence of the NRCS averaged over all azimuthal angles on atmospheric stability. Since our data contained a 60° gap in azimuth angle due to the influence of the tower, we fit the dependence of our measured NRCS values on azimuth angle to a truncated Fourier series in azimuth angle, χ:

$$\text{NRCS} = A_0 + A_1 \cos \chi + A_2 \cos 2\chi \qquad (21)$$

Using (21) in the azimuthal data gap and the actual data outside of the gap, values of NRCS could be averaged over the full 360° range.

Figures 13 through 16 show the results of plotting these averaged NRCS data against wind speed, neutral wind speed, and friction velocity for incidence angles of 20° and 40° and the two polarizations. The open diamonds in these figures correspond to data collected with z/L values between 0 and 0.12, that is, for slightly stable stratification. The asterisks indicate data collected with z/L between −0.38 and 0, or unstable conditions. In all four figures the stable data fall below the unstable data when plotted against the measured wind speed at 11.5 m. This is in agreement with the results of *Keller et al.* [1989], where the C band NRCS decreased under stable conditions.

When the same data are plotted against either u_* or $U_{N\_\text{Lake}}(19.5)$, our results indicate that the stratification dependence is rather well removed for the 40° and 60° (not shown) incidence angles but not for the 20° angle. The reason for the failure of the data to converge for the 20° incidence angle was not obvious to us. One reason may be that the 20° data represent a mixture of Bragg and specular scattering and so are more dependent on long-wave slopes than the 40° data. Thus small changes in long-wave slope caused by the slower wave growth under stable conditions may have a greater effect on 20° backscatter than on 40°; we have not attempted to remove long-wave slope effects.

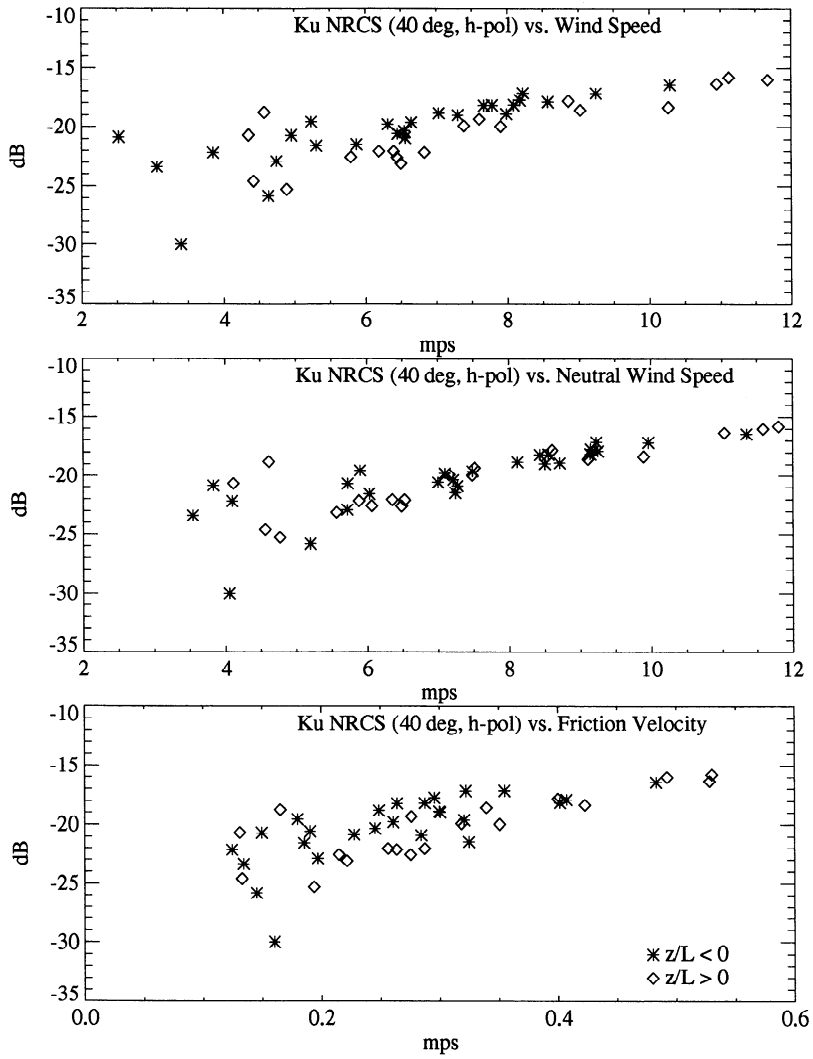

Figure 16. Azimuthally averaged, 40° incidence angle, horizontally polarized Ku band NRCS as a function of measured wind speed, neutral wind speed, and friction velocity. Diamonds correspond to NRCS values where $z/L > 0$ (stably stratified atmosphere), whereas asterisks correspond to $z/L < 0$ (unstable).

In an attempt to further define stability influences on the angular dependence of the NRCS as well as its average value, we examined the dependence of A_0, A_1, and A_2 of (21) on stability. If (21) is rewritten as follows

$$\text{NRCS} = A_0[1 + A_1/A_0 \cos \chi + A_2/A_0 \cos 2\chi] \quad (22)$$

then A_0 reflects the upwind NRCS wind speed dependence averaged over all azimuthal directions, while the ratios A_1/A_0 and A_2/A_0 reflect the downwind/upwind and cross-wind/upwind differences, respectively. The coefficients resulting from fitting the lake data with (21) are shown in Figures 17–20, in which the RADSCAT values are plotted as circles [*Donelan and Pierson*, 1987, Table 2].

At 20°, the A_0 values for vertical and horizontal polarization (V-pol and H-pol) (Figures 17a and 18a) are comparable, and the stable values are generally less than the unstable values at a given wind speed. The A_2 V-pol and H-pol values (Figures 17c and 18c) also have similar magnitude and slopes, but the stable values are now higher than the unstable values. The ratio A_2/A_0 (Figures 17e and 18e) clearly shows an atmospheric stratification effect, with the greatest values associated with the stable data. Note that while the (only) two RADSCAT A_0 and A_2 values at 20° are significantly less than the lake values, the ratio A_2/A_0 is comparable. The A_1 values are not similarly stratified by stability and are of similar magnitudes to the RADSCAT values.

The 40° vertically polarized A_0 data (Figure 19a) show a much stronger windspeed dependence than either the RADSCAT or H-pol data (Figure 20a). There is no apparent dependence on stability as was true at 20°. The same behavior holds for A_2, and A_2/A_0, (Figures 19c, 19e, 20c, and 20e). However, the A_1, and A_1/A_0 values now exhibit a stability dependence. Again, while the individual coefficients are higher on the lake than the RADSCAT data, the ratios

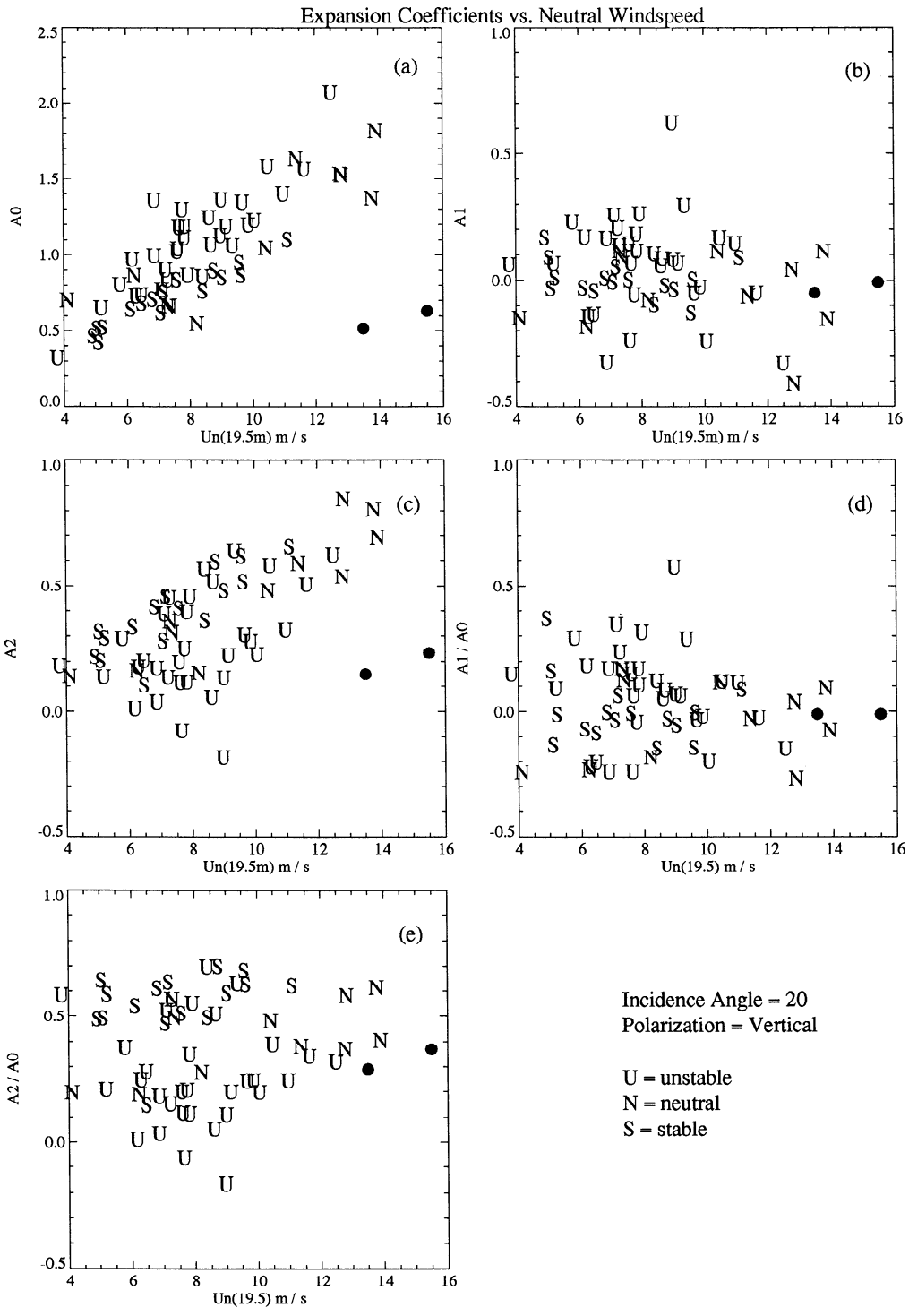

Figure 17. Azimuthal angle Fourier expansion coefficients and ratios for 20° incidence, vertically polarized data. Unstable data correspond to bulk Richardson number $Ri_B \leq -0.01$; neutral, $-0.01 \leq Ri_B \leq 0.01$; and stable, $Ri_B > 0.01$. (a) A_0, (b) A_1, (c) A_2, (d) A_1/A_0, and (e) A_2/A_0.

bracket the aircraft data, indicating that the basic sinusoidal shape of the azimuthal curves is preserved.

6. Summary and Conclusions

We have reported measurements of the normalized radar cross section for microwave backscatter from a wind-roughened water surface which were made on Lake Ontario. Simultaneous measurements of the NRCS at HH and VV polarizations from a rotating Ku band scatterometer, along with friction velocities, wind speeds, and air-water temperature differences, were obtained from the same platform. The measured drag coefficients confirmed the previously

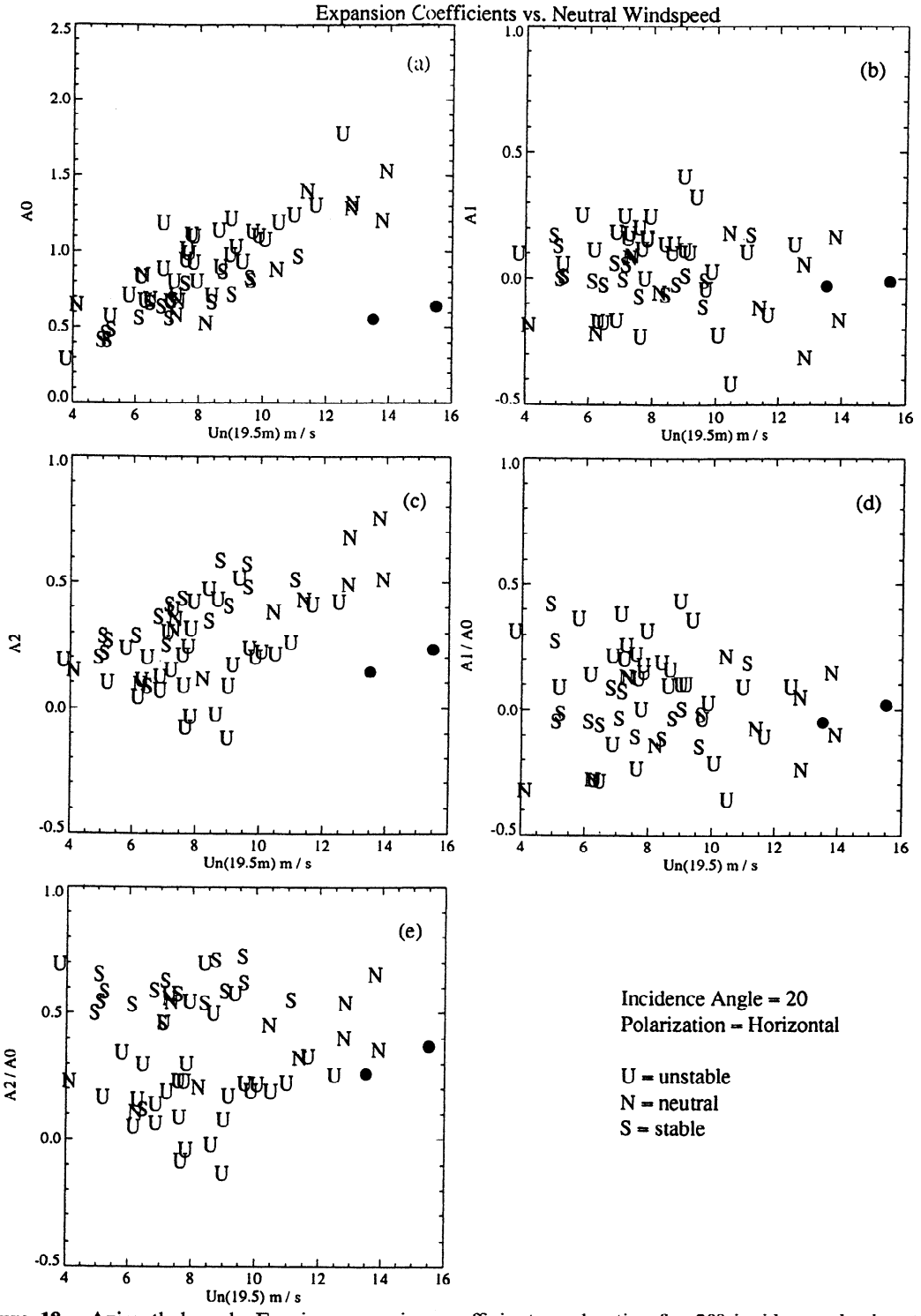

Figure 18. Azimuthal angle Fourier expansion coefficients and ratios for 20° incidence, horizontally polarized data. Unstable data correspond to bulk Richardson number, $Ri_B \leq -0.01$; neutral, $-0.01 \leq Ri_B \leq 0.01$; and stable, $Ri_B > 0.01$. (a) A_0, (b) A_1, (c) A_2, (d) A_1/A_0, and (e) A_2/A_0.

reported fact that drag coefficients on the lake are larger than those on the ocean at moderate to high wind speeds.

Under these conditions, we found the NRCS on the lake to increase with the 19.5-m neutral wind speed more rapidly than it does on the ocean for intermediate incidence angles. We showed that this behavior is more consistent with a dependence of the NRCS on wind stress or friction velocity than it is with a dependence on neutral wind speed at any height at or below 19.5 m. We found that the azimuthally integrated NRCS was nearly independent of stability when plotted against either

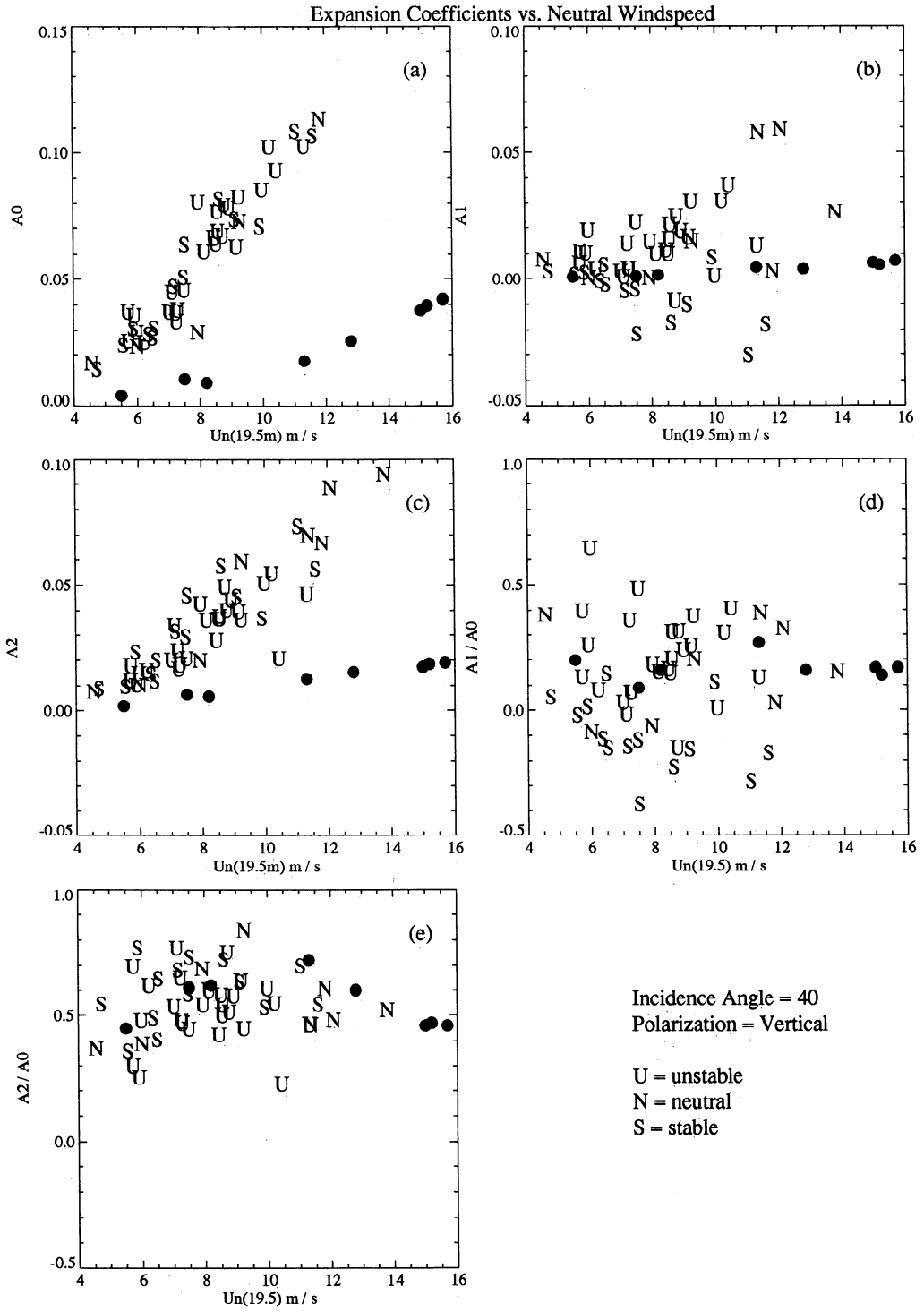

Figure 19. Azimuthal angle Fourier expansion coefficients and ratios for 40° incidence, vertically polarized data. Unstable data correspond to bulk Richardson number $Ri_B \leq -0.01$; neutral, $-0.01 \leq Ri_B \leq 0.01$; and stable, $Ri_B > 0.01$. (a) A_0, (b) A_1, (c) A_2, (d) A_1/A_0, and (e) A_2/A_0.

$U_{N\_Lake}(19.5)$ or u_* for 40° and 60° incidence angles. We did not obtain such stability independence at a 20° incidence angle, possibly owing to the involvement of long waves in the scattering process at this angle.

These results indicate that the NRCS is more closely related to the friction velocity than to the wind speed. The conversion to neutral wind speeds requires a knowledge of the drag coefficient, which, as the lake/ocean differences indicate, depends on surface wave conditions. Thus uncertainties in the drag coefficient are propagated to uncertainties in the reported neutral wind speed. Therefore we suggest that the output of satellite scatterometers should be in terms of wind stress, or friction velocity, rather than neutral wind speed.

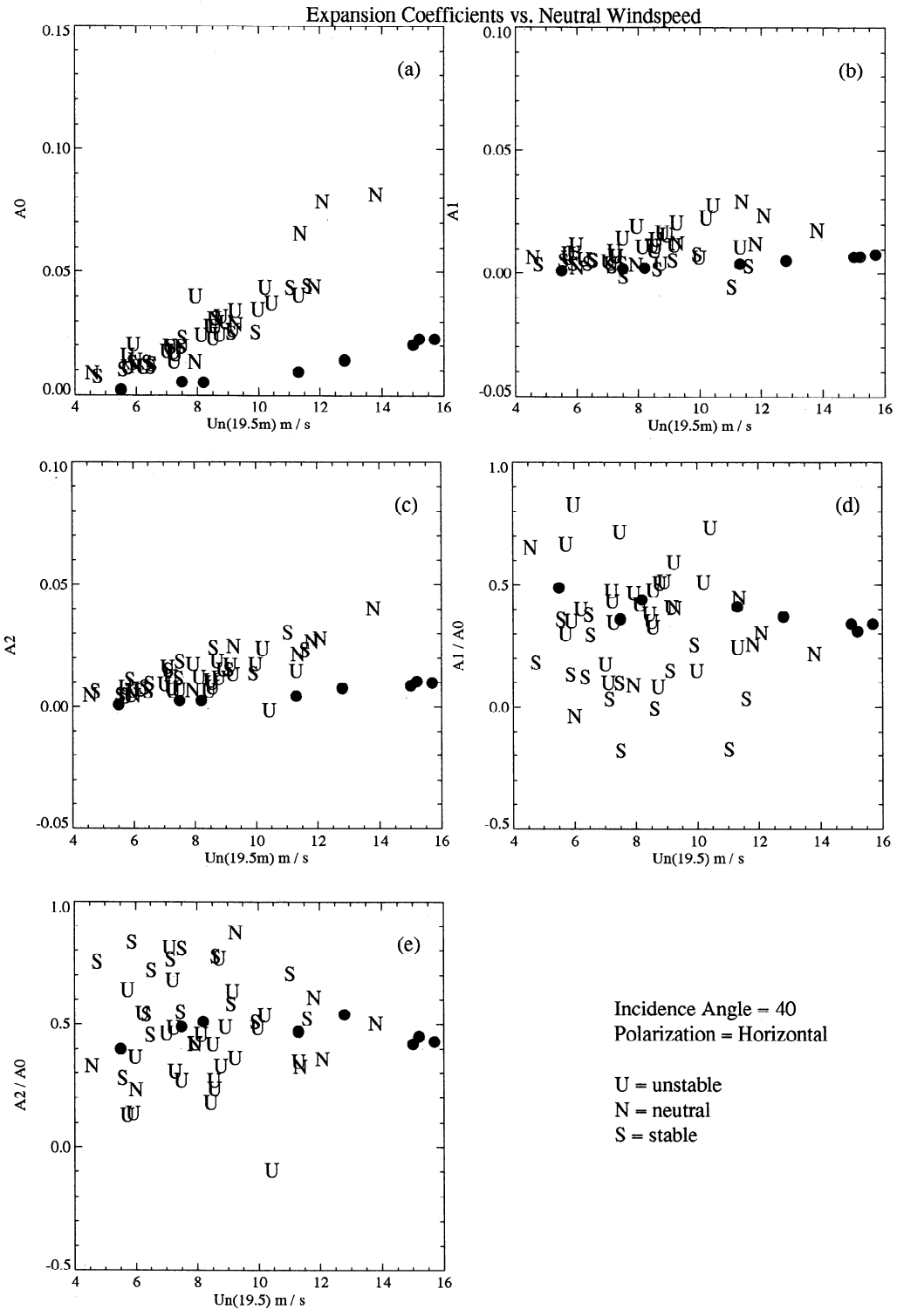

Figure 20. Azimuthal angle Fourier expansion coefficients and ratios for 40° incidence, horizontally polarized data. Unstable data correspond to bulk Richardson number $Ri_B \leq -0.01$; neutral, $-0.01 \leq Ri_B \leq 0.01$; and stable, $Ri_B > 0.01$. (a) A_0, (b) A_1, (c) A_2, (d) A_1/A_0, and (e) A_2/A_0.

Acknowledgments. The experiment described herein was executed under the direction of Mark A. Donelan at the Canadian Centre for Inland Waters, Ontario. His tutelage and hospitality and his helpful reviews of this work, are gratefully acknowledged. Special thanks are due Edward B. Thornton of the Naval Postgraduate School, Monterey, California, for exemplary service as M.C.C.'s dissertation advisor during this study. Funding for this effort was provided by the Office of Naval Technology through the Atmospheric Remote Sensing program and by grants N00014-89-J-3224 and N00014-93-I-0016 from the Office of Naval Research.

References

Askari, F., G. L. Geernaert, W. C. Keller, and S. Raman, Radar imaging of ocean fronts, *Int. J. Remote Sens.*, *14*, 275–294, 1993.

Colton, M. C., Dependence of radar backscatter on the energetics of the air-sea interface, Ph.D dissertation, 319 pp., Nav. Postgraduate Sch., Monterey, Calif., Dec. 1989.

Daley, G., W. J. Plant, D. L. Schuler, and A. C. Miller, N-ROSS scatterometer issue paper, *NRL Lett. 7910-256*, Nav. Res. Lab., Washington, D. C., 1984.

Donelan, M. A., The dependence of the aerodynamic drag coefficient on wave parameters, in *First International Conference on Meteorology and Air-Sea Interaction of the Coastal Zone*, pp. 381–387, American Meteorological Society, Boston, Mass., 1982.

Donelan, M. A., and W. J. Pierson Jr., Radar scattering and equilibrium ranges in wind-generated waves with application to scatterometry, *J. Geophys. Res.*, *92*, 4971–5029, 1987.

Donelan, M. A., N. K. Birch, and D. C. Beesley, Generalized profiles of wind speed, temperature and humidity, paper presented at 17th Conference on Great Lakes Research, Int. Assoc. Great Lakes Res., Hamilton, Ont., Canada, 1974.

Donelan, M. A., J. Hamilton, and W. H. Hui, Directional spectra of wind-generated waves, *Philos. Trans. R. Soc. London A*, *315*, 509–562, 1985.

Durden, S. L., Microwave scattering from the ocean surface, Ph.D. dissertation, *Sci. Rep. D901-1986-1*, 177 pp., Stanford Univ., Stanford, Calif., June 1986.

Durden, S. L., and J. F. Vesecky, A physical radar cross-section model for a wind-driven sea with swell, *IEEE J. Oceanic Eng.*, *OE-10*, 445–451, 1985.

Geernaert, G. L., Measurements of the angle between the wind vector and wind stress vector in the surface layer over the North Sea, *J. Geophys. Res.*, *93*, 8215–8220, 1988.

Geernaert, G. L., Bulk parameterizations for the wind stress and heat flux, in *Surface Waves and Fluxes*, vol. I, *Current Theory*, edited by G. L. Geernaert, and W. J. Plant, pp. 91–172, Kluwer Academic, Hingham, Mass., 1990.

Geernaert, G. L., K. L. Davidson, S. E. Larsen, and T. Mikkelsen, Measurements of the wind stress during the Tower Ocean Wave and Radar Dependence Experiment, *J. Geophys. Res.*, *93*, 13,913–13,923, 1988.

Hühnerfuss, H. W., W. Alpers, A. Cross, W. D. Garrett, W. C. Keller, P. A. Lange, W. J. Plant, and F. Schulde, The modification of X and L band radar signals by monomolecular sea slicks, *J. Geophys. Res.*, *88*, 9817–9822, 1983.

Jones, W. L., L. C. Schroeder, and J. L. Mitchell, Aircraft measurements of the microwave scattering signature of the ocean, *IEEE J. Oceanic Eng.*, *OE-2*, 52–61, 1977.

Jones, W. L., L. C. Schroeder, D. H. Boggs, E. M. Bracalente, R. A. Brown, G. J. Dome, W. J. Pierson, and F. J. Wentz, The Seasat-A Satellite Scatterometer: The geophysical evaluation of remotely sensed winds over the ocean, *J. Geophys. Res.*, *87*, 3297–3317, 1982.

Keller, W. C., W. J. Plant, and D. E. Weissman, The dependence of X band microwave sea return on atmospheric stability and sea state, *J. Geophys. Res.*, *90*, 1019–1029, 1985.

Keller, W. C., V. Wismann, and W. Alpers, Tower-based measurements of the ocean C band radar backscattering cross section, *J. Geophys. Res.*, *94*, 924–930, 1989.

Keller, M. R., W. C. Keller, and W. J. Plant, A wave tank study of the dependence of X band cross sections on wind speed and water temperature, *J. Geophys. Res.*, *97*, 5771–5792, 1992.

Klein, L. A., and C. T. Swift, An improved model for the dielectric constant of sea water at microwave frequencies, *IEEE Trans. Antennas Propag.*, *AP-25*, 104–111, 1977.

Large, W. G., and S. Pond, Open ocean momentum flux measurements in moderate to strong winds, *J. Phys. Oceanogr.*, *11*, 324–336, 1981.

Li, F., W. Large, W. Shaw, E. J. Walsh, and K. Davidson, Ocean radar backscatter relationship with near-surface winds: A case study during FASINEX, *J. Phys. Oceanogr.*, *19*, 342–353, 1989.

Monin, A. S., and A. M. Obukhov, Basic laws of turbulence in the ground layer of the atmosphere (in Russian), *Tr. Akad. Nauk. SSSR Geofiz. Inst.*, *151*, 163–187, 1954.

Moore, R. K., and A. K. Fung, Radar determination of winds at sea, *Proc. IEEE*, *67*, 1504–1521, 1979.

Panofsky, H. A., and J. A. Dutton, *Atmospheric Turbulence*, 397 pp., John Wiley, New York, 1984.

Pierson, W. J., Jr., The measurement of the synoptic scale wind over the ocean, *J. Geophys. Res.*, *88*, 1682–1708, 1983.

Pierson, W. J., Jr., Dependence of radar backscatter on environmental parameters, in *Surface Waves and Fluxes*, vol. II, *Remote Sensing*, edited by G. L. Geernaert and W. J. Plant, pp. 173–220, Kluwer Academic, Hingham, Mass., 1990.

Plant, W. J., A two-scale model of short wind-generated waves and scatterometry, *J. Geophys. Res.*, *91*, 10,735–10,749, 1986. (Correction, *J. Geophys. Res.*, *93*, 1347, 1988.)

Plant, W. J., Bragg scattering of electromagnetic waves from the air-sea interface, in *Surface Waves and Fluxes*, vol. II, *Remote Sensing*, edited by G. L. Geernaert and W. J. Plant, pp. 41–108, Kluwer Academic, Hingham, Mass., 1990.

Plant, W. J., and J. W. Wright, Growth and equilibrium of short gravity waves in a wind wave tank, *J. Fluid Mech.*, *82*, 767–793, 1977.

Plant, W. J., E. A. Terray, R. A. Petitt Jr., and W. C. Keller, The dependence of microwave backscatter from the sea on illuminated area: Correlation times and lengths, *J. Geophys. Res.*, *99*, 9705–9723, 1994.

Schroeder, L. C., D. H. Boggs, G. Dome, I. Halberstam, W. L. Jones, W. J. Pierson, and F. J. Wentz, The relationship between wind vector and normalized radar cross section used to derive Seasat-A scatterometer winds, *J. Geophys. Res.*, *87*, 3318–3336, 1982.

Smith, S. D., Coefficients for sea surface wind stress, heat flux, and wind profiles as a function of wind speed and temperature, *J. Geophys. Res.*, *93*, 15,467–15,472, 1988.

Snyder, R. L., F. W. Dobson, J. A. Elliott, and R. B. Long, Array measurements of atmospheric pressure fluctuations above surface gravity waves, *J. Fluid Mech.*, *102*, 1–59, 1981.

Tsanis, I., and M. A. Donelan, The WAVES programme on the CCIW research tower, *NWRI Rep. 87-65*, Res. and Appl. Branch, Canada Centre for Inland Waters, Natl. Water Res. Inst., Burlington, Ont., Canada, 1987.

Weissman, D. E., Dependence of the microwave radar cross-section on ocean surface variables: Comparison of measurements and theory using data from the frontal Air-Sea Interaction Experiment, *J. Geophys. Res.*, *95*, 3387–3398, 1990.

Wentz, F. J., S. Peteherych, and L. A. Thomas, A model function for ocean radar cross section at 14.6 GHz, *J. Geophys. Res.*, *89*, 3689–3704, 1984.

Woiceshyn, P. M., M. G. Wurtele, D. H. Boggs, L. F. McGoldrick, and S. Peteherych, The necessity for a new parameterization of an empirical model for wind/ocean scatterometry, *J. Geophys. Res.*, *91*, 2273–2288, 1986.

Wyngaard, J. C., On surface layer turbulence, in *Workshop on Micrometeorology*, edited by D. A. Haugen, pp. 101–150, American Meteorological Society, Boston, Mass., 1973.

M. C. Colton, Satellite Division, Code 73, Fleet Numerical Meteorology and Oceanography Center, 7 Grace Hopper Road, Stop 1, Monterey, CA 93943. (e-mail: mcolton@fnoc.navy.mil)

G. L. Geernaert, Division of Emissions and Air Pollution, National Environmental Research Institute, Frederiksborgvej 399, DK-4000 Roskilde, Denmark.

W. C. Keller and W. J. Plant, Applied Physics Laboratory, University of Washington, Seattle, WA 98105.

(Received May 27, 1994; revised January 31, 1995; accepted January 31, 1995.)